
ADAPTIVE PHYSICS-INFORMED NEURAL OPERATOR FOR COARSE-GRAINED NON-EQUILIBRIUM FLOWS

Ivan Zanardi

Center for Hypersonics and Entry Systems Studies (CHESS)
University of Illinois Urbana-Champaign
Urbana, IL, 61801, USA
zanardi3@illinois.edu

Simone Venturi

Center for Hypersonics and Entry Systems Studies (CHESS)
University of Illinois Urbana-Champaign
Urbana, IL, 61801, USA
sventuri@illinois.edu

Marco Panesi

Center for Hypersonics and Entry Systems Studies (CHESS)
University of Illinois Urbana-Champaign
Urbana, IL, 61801, USA
mpanesi@illinois.edu

ABSTRACT

This work proposes a new machine learning (ML)-based paradigm aiming to enhance the computational efficiency of non-equilibrium reacting flow simulations while ensuring compliance with the underlying physics. The framework combines dimensionality reduction and neural operators through a hierarchical and adaptive deep learning strategy to learn the solution of multi-scale coarse-grained governing equations for chemical kinetics. The proposed surrogate's architecture is structured as a tree, where the leaf nodes correspond to separate physics-informed deep operator networks (PI-DeepONets). The hierarchical attribute has two advantages: i) It allows the simplification of the training phase via transfer learning, starting from the slowest temporal scales; ii) It accelerates the prediction step by enabling adaptivity as the surrogate's evaluation is limited to the necessary leaf nodes based on the local degree of non-equilibrium of the gas. The model is applied to the study of chemical kinetics relevant for application to hypersonic flight, and it is tested here on a pure oxygen gas mixture. The proposed ML framework can adaptively predict the dynamics of almost thirty species with a relative error smaller than 4% for a broad range of initial conditions. This work lays the foundation for constructing an efficient ML-based surrogate coupled with reactive Navier-Stokes solvers for accurately characterizing non-equilibrium phenomena.

Keywords · Physics-informed machine learning · Neural operators · DeepONet · Multi-scale surrogates · Multi-fidelity · Hypersonic flow · Thermochemical non-equilibrium · Coarse-graining

1. Introduction

Accurate modeling of non-equilibrium reacting flows is critical in many engineering and science disciplines, *e.g.*, designing hypersonic vehicles for space exploration [1, 2] or material processing and manufacturing with low-temperature plasmas [3, 4]. The need for describing and understanding these flows has led to the development of increasingly large and sophisticated mathematical models [5–8], describing multiple physical phenomena characterized by a broad spectrum of spatio-temporal scales.

The most physically consistent approach to model non-equilibrium flows relies on the direct numerical solution of the master equation [5, 6, 9–13], whereby all the relevant spatial and temporal scales resulting from chemical and radiative processes are accounted for. Indeed, the availability of quantum state-to-state (StS) chemistry models based on *ab initio* theories [14–18] enables unprecedented levels of physical accuracy [5–8], crucial for modeling flows typified by a significant degree of non-equilibrium. However, the exponentially large number of degrees of freedom (*i.e.*, molecules’ and atoms’ energy levels) and the numerical restrictions (stiffness) associated with the derived system of equations make these models impracticable in large-scale multi-dimensional CFD problems. To overcome these difficulties, crude “engineering” non-equilibrium models [19, 20], referred to as multi-temperature (MT) models, have been developed over the years, often assembled without any rigorous derivation from fundamental kinetic equations nor consideration for physical principles and constraints. Given their interpolative nature, these cannot be used to perform predictions outside their development range.

This work targets the numerical challenges in solving such computationally intense systems of equations by surrogating the thermochemical processes characterizing non-equilibrium phenomena that conventional techniques cannot address. Surrogate and reduced-order models [21–26] can be designed and constructed by employing various techniques, such as projection-based methods [27–33], data-fit interpolation and regression [34], and machine learning (ML)-based models [35, 36]. A recent application of surrogate models for hypersonics has been published by Ozbenli *et al.* [37], who trained a feed-forward neural network (FNN) to learn a given set of the master equations’ solution functions for a specific non-equilibrium model [38]. Their ML framework showed a great computational speed-up compared to numerical integrators, with generalization performances left unclear. Similarly, Campoli *et al.* [39] explored different ML algorithms to regress the source terms of the ODEs system modeling the thermochemical relaxation processes. A coupling between a conventional integrator and the ML regressor was attempted, and speed-up performances were analyzed. They also tried to infer the solution of Euler’s equations for a single one-dimensional reacting shock flow scenario by leveraging a deep neural network (DNN). Scherding and coworkers [40], instead, developed a lower-dimensional surrogate to compute the thermochemical properties of the gas mixture to be used in place of any high-dimensional look-up non-equilibrium thermodynamic library. However, despite the considerable speed-up performances and encouraging perspective, they did it only for steady-state solutions, targeting specific flow conditions and considering only chemical and not thermal non-equilibrium. The above-mentioned frameworks lack generalization performances and do not impose physical constraints during the surrogate construction, making them less suitable for CFD simulations. Instead, the present study aims to provide a prototyping tool that can replace the master equations with a surrogate model that preserves the original’s essential properties and physical constraints while being orders of magnitude faster and able to cover an extensive range of physical conditions. The present work augments the framework introduced by Zanardi *et al.* [41], and it introduces a new machine learning-based method for solving non-equilibrium flows by combining:

- Coarse-graining, *i.e.*, a reduced order modeling (ROM) technique that extracts meaningful physics from the master equations [10, 42–45], in general, by leveraging unsupervised learning adaptation to seek the optimal grouping configuration [46]. The so-derived reduced system of equations models the dynamics of groups of states, addressing the high-dimensionality problem characterizing the StS models.
- Neural operators, *i.e.*, a ML-constructed surrogate that approximates the integral solution operator of a family of partial differential equations (PDEs) to bypass conventional numerical integration [47].

Coarse-graining. Constructing a surrogate for high-fidelity quantum-state-specific chemistry models to describe non-equilibrium phenomena is not a simple task as they rely on the solution of an overwhelmingly large number of differential equations (order of 10^5) [5]. More importantly, the mathematical closure of these equations requires the determination of a sizeable kinetic database that often cannot be computed owing to many processes (order of 10^{16}) to be considered. Therefore, performing first a physics-preserving dimensionality reduction is of paramount importance. To this end, nonlinear manifold learning techniques such as autoencoders [48], diffusion maps [49], or kernel PCA [50] could be employed. Recently, Oommen *et al.* [51] proposed learning high-dimensional complex dynamics by combining neural operators and autoencoders. Their application first reduced the problem’s dimensionality by training a convolutional autoencoder and then learned the low-dimensional dynamics lying in the latent space using a deep neural operator. However, although powerful in applications requiring dimensionality reduction, autoencoders lack physical interpretability and introduce spurious correlations, not necessarily guaranteeing a discrete separation of temporal scales. To overcome these limitations, our approach relies on a class of physics-based reduced-order coarse-grained (CG) models [52–54]. In chemical kinetics, coarse-grained modeling has extensively been used to describe non-equilibrium phenomena of atomic and molecular species [45, 46, 55–58]. The central idea in the proposed CG model is to combine the solution of the coarse-grained dynamics with the partial equilibration of the underlying microscopic structure. The concept of partial equilibrium suggests applying the *maximum entropy principles* to reconstruct the unresolved scales or

physics. This choice is of paramount importance, as it ensures the physical consistency of the model by enforcing the *principle of detailed balance* and ensuring the positivity and boundness of the distribution function.

Neural operators. The second basis of the proposed methodology aims to address the stiffness associated with thermochemical processes, characterized by a broad spectrum of temporal scales, ranging from the flow time scales to time scales that are orders of magnitude smaller. This work uses DNNs to infer the generalized solution of the governing equations to bypass the conventional numerical integration. In literature, a series of new ML-based paradigms for speeding up the numerical simulation of partial differential equations [59–65] have been proposed over the past few years. In particular, this work leverages the family of neural operators¹ [47, 66–70], DNN-based surrogates able to learn solution operators defined by the mapping between inputs of a dynamical system, such as initial or boundary conditions (ICs/BCs), and its state. We employ a parametric-based approach to operator learning, introduced first by Chen *et al.* [71] and then recently extended by Lu *et al.* [72]. In their work, Lu and coworkers constructed a new network architecture called deep operator network (DeepONet), which has shown effectiveness in approximating the solution operator of linear and non-linear parametric PDEs². DeepONets have been employed in different fields of physics, such as modeling electroconvection phenomena [73], closure problems for turbulence-chemistry interactions in turbulent combustion framework [74], surrogating molecular dynamics in reacting gas mixtures [75], and modeling brittle fracture [76]. In hypersonics, Mao *et al.* [77] used DeepONet to approximate the fluid flow evolution and concentration profiles downstream of a normal shock in hypersonic conditions. While important for the scientific community, the work of Mao and coworkers relies on a simple physical model that cannot correctly represent the non-equilibrium distribution of the internal energy states, which is central to this work. Additionally, Mao *et al.*'s work does not enforce physics constraints during training, biasing the ML model towards physically consistent solutions. Instead, this work relies on physics-informed (PI) machine learning methodologies [78–83], also referred to as PINNs, whereby physics constraints are imposed by penalizing the departure from governing equations during the training phase of the model. PI techniques can improve the model generalization performances since they employ physical constraints in the loss functions. This ML class, named physics-informed deep neural operator (PI-DeepONet) [84–87] and combining PI techniques and the DeepONet architecture, was first developed by Wang *et al.* [84] and applied to the construction of surrogate solution operators of different PDEs showing excellent results.

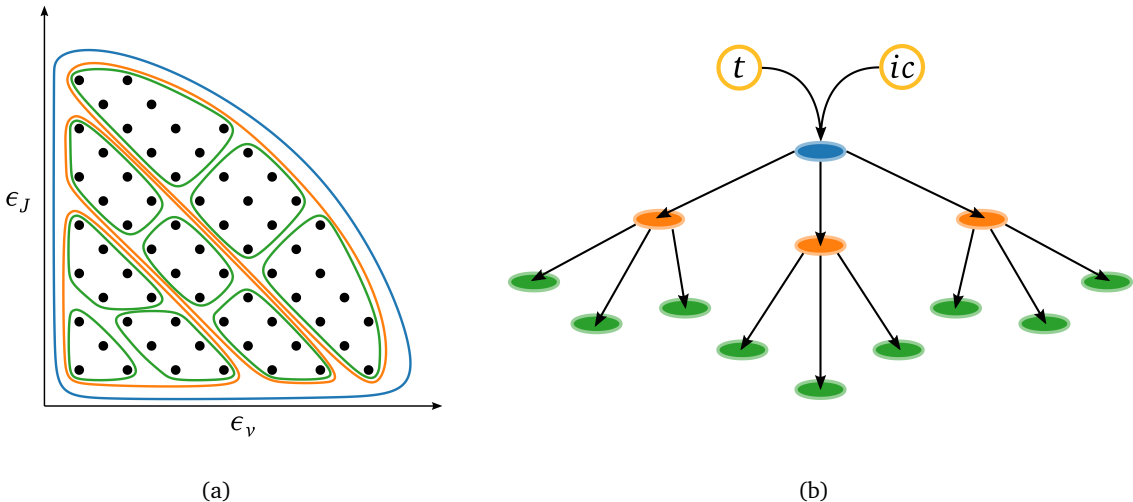


Figure 1. *Schematics of the proposed approach.* Combining coarse-graining (a) and hierarchical DeepONets (b). (a) Reduced order modeling technique based on clustering the species' quantum energy states (schematized as black dots and as functions of vibrational, ϵ_v , and rotational energy, ϵ_J) into macroscopic bins. In the figure, three different levels of hierarchical clustering are shown. (b) Tree visualization of the hierarchical deep learning framework, where the leaf nodes correspond to separate DeepONets (one for each macroscopic bin), which take as inputs the initial conditions, ic , and time, t .

Proposed approach. The combined use of coarse-graining and neural operators in the form of DeepONets is of primary importance. On the one hand, the mere application of neural operators does not resolve the high-

¹Generalization of neural networks for designing/learning solution maps between function spaces, *e.g.* approximating the integral solution operator of a family of PDEs.

²The terminology “parametric PDEs” refers to the fact that some parameters of the given PDE system, like initial conditions or reaction rates, are allowed to vary over a certain range.

dimensionality problem, as it is not straightforward to design and train an efficient surrogate for thousands of coupled differential equations. On the other hand, dimensionality reduction does not solve the issues with integration, as small steps are still needed to stably integrate the reduced system of equations. For these reasons, the proposed framework is characterized by a novel physics-inspired architecture based on a series of hierarchical DeepONets used to learn the solution operator for multiple coarse-grained configurations to resolve different scales of the phenomena considered. The CG surrogate model herein proposed, referred to as CG-DeepONet throughout the rest of the paper, is constructed by training each scale sequentially and employing transfer learning between these. In this sense, our framework is in line with recent operator learning techniques for multi-scale systems [88–93]. Among the latest ones, Liu *et al.* [88] proposed a hierarchical time-steppers approach to the solution of the dynamics by constructing multiple neural networks trained to capture the various timescales by varying the integration step. We also recall the work of Migus *et al.* [89], who designed a multi-scale architecture based on multi-pole graph neural operators (MGNO) by embedding multi-resolution iterative methods [94]. Liu and coworkers [90] took inspiration from the celebrated hierarchical matrix methods to develop their multi-scale hierarchical transformer. Moreover, Liu and Cai [91] embedded multi-scale deep neural networks (MscaledNNs) [95] inside the DeepONet architecture.

Our proposed architecture allows the development of a parsimonious and autonomous tool that can quickly deliver the optimal thermochemical representation of the gas given initial conditions and time instant by adaptively choosing the most efficient and physically accurate grouping resolution. The need for adaptation is a direct consequence of different physical scenarios arising in multidimensional numerical simulations, ranging from equilibrium or near-equilibrium to strong non-equilibrium conditions. Consistently, our approach operates in the space of the discrete energy states (*i.e.*, quantum states), and it autonomously lumps together only states that are likely to be found in local equilibrium [46, 57]. A controller-like surrogate, identified as Neq-DeepONet in the remainder of this paper, is responsible for the model adaption to the local flow conditions, making our surrogate suitable for multi-fidelity predictions. In this sense, our framework can be viewed as a multi-fidelity composition of DeepONets and shares analogies with some recent works on the topic [96–98]. However, the novelty of our approach stems from the definition of such a composition based on the maximum-entropy coarse-graining, which is consistent with the underlying physics.

The methodology is here tested for O₂–O kinetics, but it can be easily extended to other chemical mixtures or even to other physical problems experiencing a broad spectrum of temporal or spatial scales.

The paper is organized as follows. First, Sec. 2.1 provides the basic framework and derivation of the thermochemical non-equilibrium model. Then, descriptions of the proposed ML framework and the developed adaptive technique are presented in Sec. 2.2 and Sec. 2.3, respectively. In Sec. 3, different aspects of the surrogate model and the adaptive method are illustrated and discussed in detail. Finally, Sec. 4 presents the concluding remarks and possibilities for future work. The interested reader can find further information in the Supplementary Materials.

2. Methodology

2.1. Physical modeling

Modeling of chemically reacting flows relies on the solution of Navier-Stokes equations complemented by additional conservation equations accounting for changes in the chemical composition and non-equilibrium relaxation of the energy modes. This extra set of equations often represents a computational burden that makes reacting non-equilibrium flows hard to solve. An extensive discussion on non-equilibrium modeling can be found in Ref. [45].

The most general way to express the governing equations is

$$\frac{D}{Dt} (\rho_i e_i^m) + \nabla \cdot \mathcal{J}_i^m = \Omega_i^m, \quad (1)$$

where ρ_i and e_i indicate the mass density and the energy per unit mass of the i -th pseudo-species, m the moment order (0, 1, 2, *etc.*), and Ω_i the reactive source terms. D/Dt is the Lagrangian derivative and \mathcal{J}_i^m the dissipative/diffusion terms. Depending on the assumptions made in the definition of the chemical species indicated by i , three different models can be identified:

- i. If i refers to a particular energy state (*i.e.*, rovibronic $\rho_i(e_i, v_i, J_i)$), the approach is called state-to-state (StS) master equations [5, 6]. In this case, m is set to 0.
- ii. If ρ_i indicates the density of a group of states, the approach is named coarse-grained (CG) modeling or coarse-grained master equations (CGME) [42, 45, 46, 57, 58, 99–101]. In this case, the conservation equations for mass, momentum, and energy are complemented by additional equations (*i.e.*, $m = 1$ and/or $m = 2$) to model internal energy modes and chemical composition.
- iii. In the case of binning one group per internal energy mode, which is a particular case of (ii), we have the multi-temperature (MT) models [102].

Fig. 2 highlights the different physical accuracy and resolution of the three models mentioned above. A substantial loss of physical information can be noticed moving from the internal energy states distribution obtained with the StS model to the one defined by Park’s two-temperature model [102], which is a particular case of the MT models, where all the states are collapsed along a straight line. Differently, the CGME approach better captures the StS distribution by modeling the dynamics of multiple clusters of states (27 in Fig. 2, namely the CGME27 model). In this work, only the coarse-grained master equations approach will be employed to construct our surrogate.

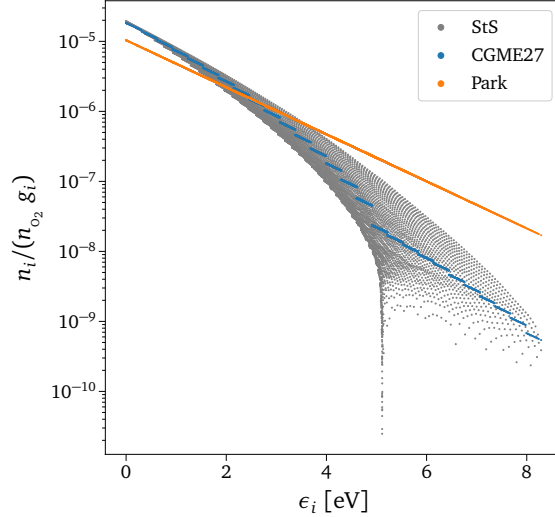


Figure 2. Normalized quasi-steady state (QSS) rovibrational states distribution for different models. The orange dots are determined by Park’s two-temperature model, *e.g.*, a particular MT model, the blue ones by the 27-groups CG grouping strategy, and the grey ones by the StS modeling. Initial conditions used: $P_0 = 1\,000$ Pa, $X_{O_0} = 0.05$, $T_{int0} = 1000$ K, $T = 15\,000$ K.

2.1.1. Coarse-grained modeling

The numerical solution of the master equations, whereby the dynamics of each internal energy state is captured via the direct solution of the corresponding mass conservation equations, is often impractically expensive. Moreover, it is usually not required since the internal energy distribution is generally found as a composition of partial equilibria rather than a complete non-equilibrium state [46]. The concept of local or partial equilibrium suggests the application of the *principle of maximum entropy* to reconstruct the unresolved scales of physics [10, 44, 45]. The construction of a coarse-grained model is accomplished by adopting a two-step procedure which goes as follows [103]:

- i. group energy states into \mathcal{N}_g macroscopic bins according to a specific strategy;
- ii. prescribe a bin-wise distribution function to represent the population within each group together with a series of moment constraints.

This work employs a log-linear form for the bin-wise distribution function, which results in a thermalized local Boltzmann distribution within individual bins, defined as follows

$$\mathcal{F}_p^i(\epsilon_i): \quad \log\left(\frac{g_i}{n_i}\right) = \alpha_p + \beta_p \epsilon_i, \quad (2)$$

where the bin-specific coefficients α_p and β_p are expressed in function of the macroscopic group constraints (*i.e.*, number density, energy, *etc.*). The total population and energies of the different bins are the set of unknowns for the reduced-order system. The governing equations for these macroscopic constraints can be derived by taking successive moments of the StS master equations, using $(\epsilon_i)^m$ for $m = 0, 1, \dots$ as weights (see Sec. S.1 of the Supplementary Materials for more details).

While more accurate strategies have been developed during the past few years [46, 57], the model-reduction approach employed in this work is the rovibrational energy-based grouping technique (RVE) [100, 101], which lumps together energy states with similar internal energy regardless of their rotational and vibrational quantum numbers.

2.1.2. Test case: ideal chemical reactor

We wish to investigate the behavior of oxygen molecules in their electronic ground state undergoing dissociation when subjected to sudden heating in an ideal chemical reactor. We make the following assumptions:

- i. The 0-D reactor is plunged into a thermal bath maintained at constant temperature T .
- ii. The translational energy mode of the atoms and molecules is assumed to follow a Maxwell-Boltzmann distribution at the temperature T of the thermal bath.
- iii. At the beginning of the numerical experiment, the population of the rovibrational energy levels is assumed to follow a Boltzmann distribution at the internal temperature T_{int_0} .
- iv. The volume of the chemical reactor is kept constant during the experiment, and the thermodynamic system is closed (no mass exchange with the surrounding environment).
- v. Only α_p in Eq. (2) is modeled for each bin P , while $\beta_p = 1/(k_B T_p)$ is kept constant during the 0-D simulation, with k_B being the Boltzmann's constant and $T_p = T$.

Therefore, Eq. (1) reduces to

$$\begin{aligned} \frac{d\rho_i}{dt} &= \Omega_i^0(\rho_i, T) , \\ \rho_i(t=0) &= f_i \end{aligned} \quad (3)$$

where f_i refers to the corresponding Maxwell-Boltzmann equilibrium value of specie i at temperature T_{int_0} .

Since the goal is to learn the integral solution operator of the rovibrational CG master equations to be able to deliver accurate predictions in multidimensional CFD simulations characterized by a wide range of physical scenarios, we aim to generalize over the space of initial conditions (ICs) and time domain. The ICs are generated by defining the initial pressure P_0 , the initial molar fraction of atomic oxygen X_{O_0} , the translational temperature T , and the initial internal temperature T_{int_0} for which a Boltzmann distribution is prescribed for the O_2 bins. In this work, the domain in which the initial conditions have been sampled is defined in Tab. 1 as minimum-maximum pair values. For all the possible sampling scenarios, T is greater than T_{int_0} , which implies that thermal excitation and dissociation processes are the dominant phenomena occurring in the reactor.

	P_0 [Pa]	X_{O_0}	T_{int_0} [K]	T [K]
Min	1 000	0	1 000	8 000
Max	10 000	0.95	8 000	15 000

Table 1. *Space of initial conditions.* Minimum-maximum pair values for each IC variable.

Regarding the time domain, we train the model over an interval of $[0, 10^{-2}]$ s, covering most excitation and dissociation processes for the non-equilibrium problem under investigation.

2.2. Neural operators

2.2.1. DeepONet

Building upon the original formulation of the DeepONet by Lu *et al.* [72], whereby the solution operator G maps an input function \mathbf{u} and the continuous coordinates \mathbf{y} of $G(\mathbf{u})$ to a real scalar value, this work extends the DeepONet framework to accommodate the high-dimensional nature of the master equations, thus obtaining an output vector $\mathbf{G}(\mathbf{u})(\mathbf{y}) \in \mathbb{R}^D$, where D is the number of the output variables [41, 67]. As illustrated in Fig. 3, the original DeepONet architecture is characterized by two different deep neural networks: the ‘‘branch net’’ and the ‘‘trunk net’’. The modified version is characterized by multiple branches, one for each output variable, which takes \mathbf{u} as input and returns a feature embedding $\boldsymbol{\alpha} \in \mathbb{R}^p$ as output. Instead, the trunk net takes the continuous coordinates \mathbf{y} as inputs and outputs another feature embedding $\boldsymbol{\phi} \in \mathbb{R}^p$. This block is shared between different branches [67, 104], gaining computational efficiency. In the framework of operator learning for ODEs, \mathbf{u} represents the space of initial conditions, whereas \mathbf{y} is the time variable. To obtain a continuous and differentiable representation of the output functions of the DeepONet, the outputs of each branch and the trunk networks are merged via a dot product as follows

$$\widehat{\mathbf{G}}^{(i)}(\mathbf{u})(\mathbf{y}) = \sum_{k=1}^p \alpha_k^{(i)}(\mathbf{u}) \phi_k(\mathbf{y}) . \quad (4)$$

One can notice that Eq. (4) reminds the proper orthogonal decomposition (POD) formulation [105], as highlighted by Lu *et al.* in Ref. [67], and more generally Eq. (4) can be related to the singular value decomposition (SVD)

factorization, as explained by Venturi and Casey [104]. From this perspective, the trunk net learns the p most importation modes of the dynamical system, ϕ , while the branch net learns the coefficients α of the expansion. Under this perspective, the shared-trunk version of the DeepONet works reasonably well only when the dynamics of the modeled variables are similar to each other such that they can share the same basis ϕ [104].

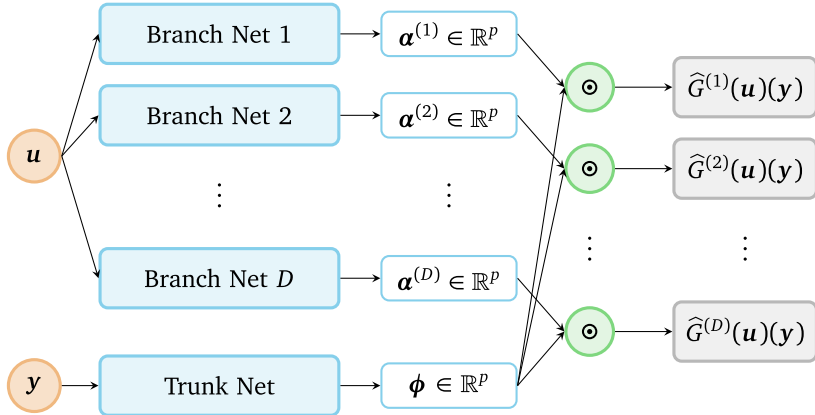


Figure 3. *Multi-output DeepONet*. The modified architecture consists of multiple “branch nets” (one for each output) for extracting latent representations of the input functions and one “trunk net” for extracting latent representations of the input coordinates at which the output functions are evaluated.

2.2.2. Multi-scale hierarchical coarse-grained model

Similar to what is done in adaptive mesh refinement (AMR) techniques used in CFD, the accuracy of the CG model can be improved by increasing the number of groups but at a higher computational cost. The improvement in accuracy is explained by the larger range of scales (or kinetic processes) that can be resolved. Indeed, taking as an example the rovibrational energy-based grouping strategy employed in this work, if we recursively split the energy space of the internal states by following a cascade in the groups, all the micro-groups inside the corresponding macro-group quickly reach the same equilibrium value, showing a fast dynamical behavior. Consistently, we leveraged the multi-scale nature of the physical problem to construct a physics-inspired ML-based surrogate model (see Sec. S.2 of the Supplementary Materials for all the details) by sequentially learning the different timescales of the thermochemical phenomena occurring inside a 0-D reactor.

- *Timescale 1*

Chemical dissociation of O_2 molecules (irrespective of their internal excitation) and creation of O atoms are the slowest processes that can be learned. As shown in Fig. 4(a), the outputs of the DeepONet employed for this first timescale, denominated as CG-DeepONet^(1,1) (i.e., the surrogate’s component in charge of predicting the group number one in the scale number one), are simply the mass fractions of O and O_2 . So, we are assuming that all the internal states can be clustered in one unique group [see Fig. 4(b)], but we do not solve for the rovibrational-translation energy transfer phenomena. As concerns the physical input of the model, \mathbf{u} represents the initial conditions of the reactor, which is characterized by translational temperature, T , reactor density, ρ , and initial mass fraction of O_2 , while the independent variable, \mathbf{y} , of the operator $\mathbf{G}(\mathbf{u})$ is the time, t :

$$\begin{aligned} \mathbf{u} &= [T, \rho, Y_{O_2}] && \in \mathbb{R}^3 \\ \mathbf{y} &= t && \in \mathbb{R}^1 \\ \widehat{\mathbf{G}}(\mathbf{u})(\mathbf{y}) &= [\widehat{Y}_{O|u}(t), \widehat{Y}_{O_2}^{(1,1,1)}|u(t)] && \in \mathbb{R}^2 \end{aligned} \tag{5}$$

In (5) and Fig. 4(a), a series of two or three superscripts have been used, where the first one corresponds to the *timescale* investigated, the second the DeepONet *index*, and the last one the O_2 *group*. They will help to identify the different variables and DeepONets used for each timescale. The *Softmax* function in Fig. 4(a) is applied to the dot product outputs after these are linearly transformed. It guarantees the mass fractions to be positive values and the mass to be conserved.

- *Timescale 1-2*

In the following timescale, we start modeling the energy exchange processes for O_2 . To do so, the internal states are clustered into three groups (CGME3) which is equivalent to uniformly splitting the energy space

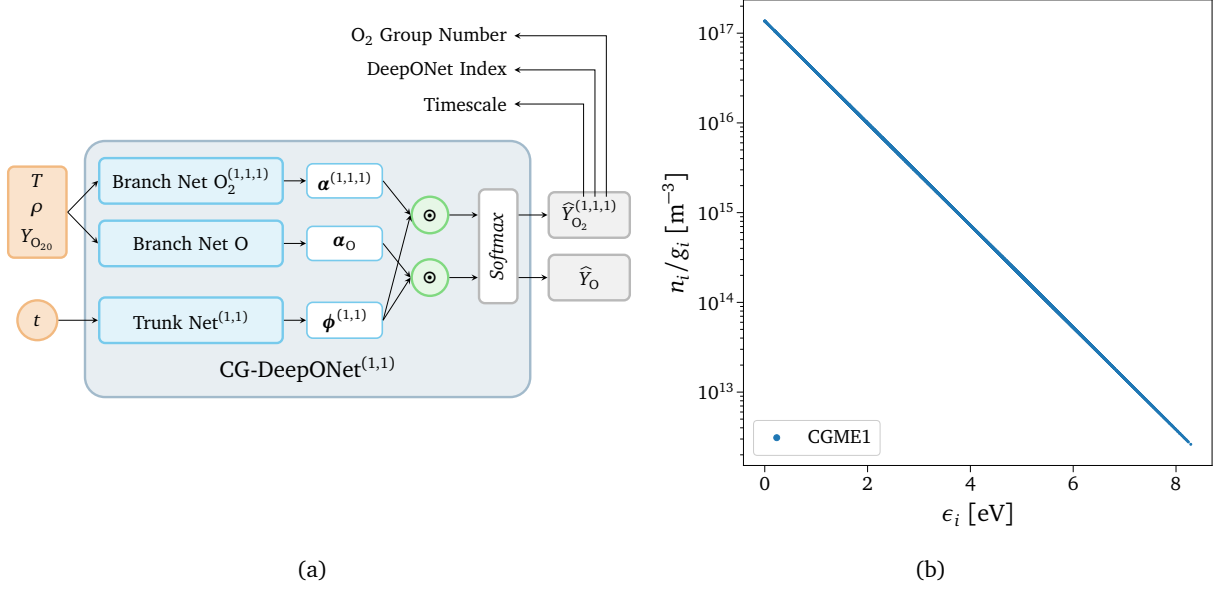


Figure 4. *Timescale 1*. Surrogate for 1-group CG master equations (CGME1). (a) Schematics of the network architecture. (b) O_2 rovibrational distribution for 1-group rovibrational CG grouping.

covered by the unique group from the previous timescale (CGME1) into three parts, as shown in Fig. 5(b). To learn the dynamics of this new system, the information learned from the previous timescale is leveraged by adopting transfer learning for the calibrated weights of $CG-DeepONet^{(1,1)}$. The new DeepONet is designed to learn only the 3-groups normalized distribution. The actual mass fractions of the three bins are then obtained by multiplying the modeled distribution by the total mass fractions of O_2 predicted by $CG-DeepONet^{(1,1)}$, as shown in Fig. 5(a). In terms of architecture, two are the difference between *Timescale 1* and *Timescale 2*.

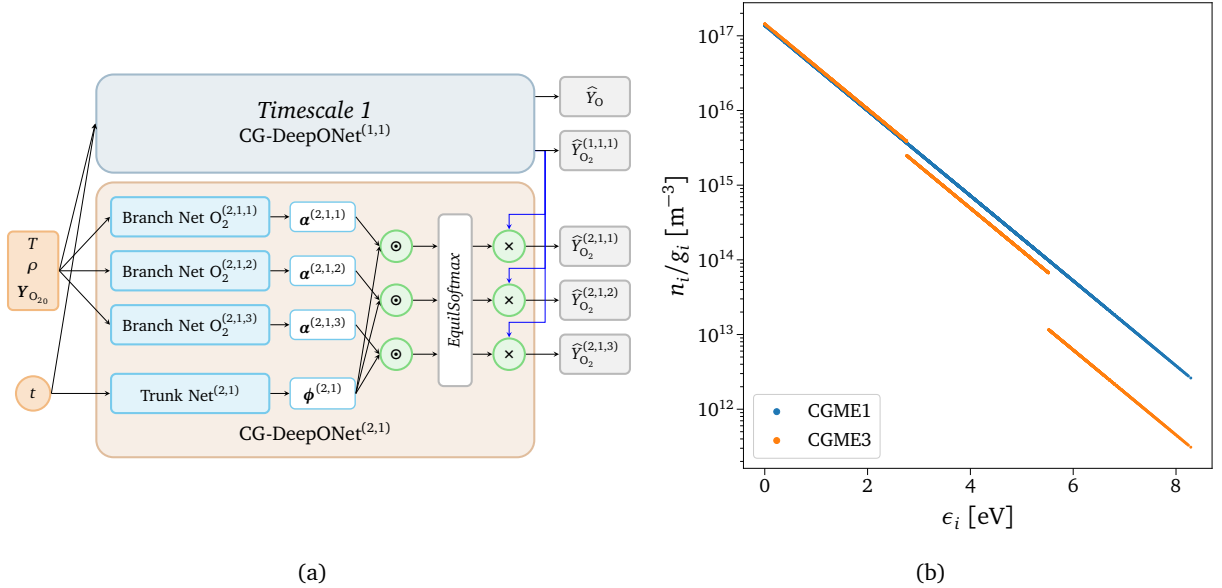


Figure 5. *Timescale 1-2*. Surrogate for the 3-groups CG master equations. (a) Schematics of the network architecture. (b) O_2 rovibrational distribution for 1-group (CGME1) and 3-groups (CGME3) CG grouping.

The first is related to the inputs, \mathbf{u} , of the branch net, which considers the initial mass fractions of all the three groups, $Y_{O_{20}}$. Since *Timescale 1* takes as an input the total mass fraction of O_2 as described in (5), the three values are summed to get the correct input for $CG-DeepONet^{(1,1)}$. The second aspect concerns the replacement of the *Softmax* layer with the *EquilSoftmax* one. The latter can be considered as an extension of

the former, and it has the following formulation:

$$\frac{\widehat{Y}_{O_2}^{(2,1,i)}}{\widehat{Y}_{O_2}^{(1,1,1)}} = \text{EquilSoftmax}(\mathbf{x})_i = \frac{\exp(x^{(2,1,i)})Q_i(T)}{\sum_i \exp(x^{(2,1,i)})Q_i(T)} \quad \text{for } i = 1, 2, 3, \quad (6)$$

where $Q_i(T)$ is the internal partition function of group i . Therefore, if $x^{(2,1,i)} = 0 \forall i$, all the groups are in equilibrium at the translational temperature T , which is provided as one of the inputs \mathbf{u} . Since the surrogate is informed *a priori* by the groups' equilibrium distribution function, the combined training of *Timescale 1* and *Timescale 2* is faster. Indeed, at initialization, the surrogate can already predict reasonable physical solutions if the weights of CG-DeepONet^(2,1) are zero-initialized. It has to be highlighted that all the parameters of CG-DeepONet^(1,1) are re-trained together with the ones of CG-DeepONet^(2,1), rather than being kept frozen.

- *Faster Timescales*

It is possible to increase the accuracy of the CG model by further splitting the energy space into a higher number of clusters. Therefore, by sequentially repeating the same procedure that has been done for augmenting the model from *Timescale 1* to *Timescale 2*, we can construct a surrogate that can predict the dynamics of high-resolution CG models. In our case, we further split each bin into three more bins, obtaining first a 3-group CG modeling for *Timescale 2*, then a 9-group CG modeling for *Timescale 3*, and finally a 27-group CG modeling for *Timescale 4*. We treat each group's triplet with a single DeepONet, and we apply the *EquilSoftmax* layer at the output of each entire timescale block. As explained in the previous paragraph, the predicted mass fraction of each macro-group multiplies the distribution of the corresponding three micro-groups, obtaining a hierarchical surrogate for multi-scale coarse-grained dynamics, as shown in Fig. 6.

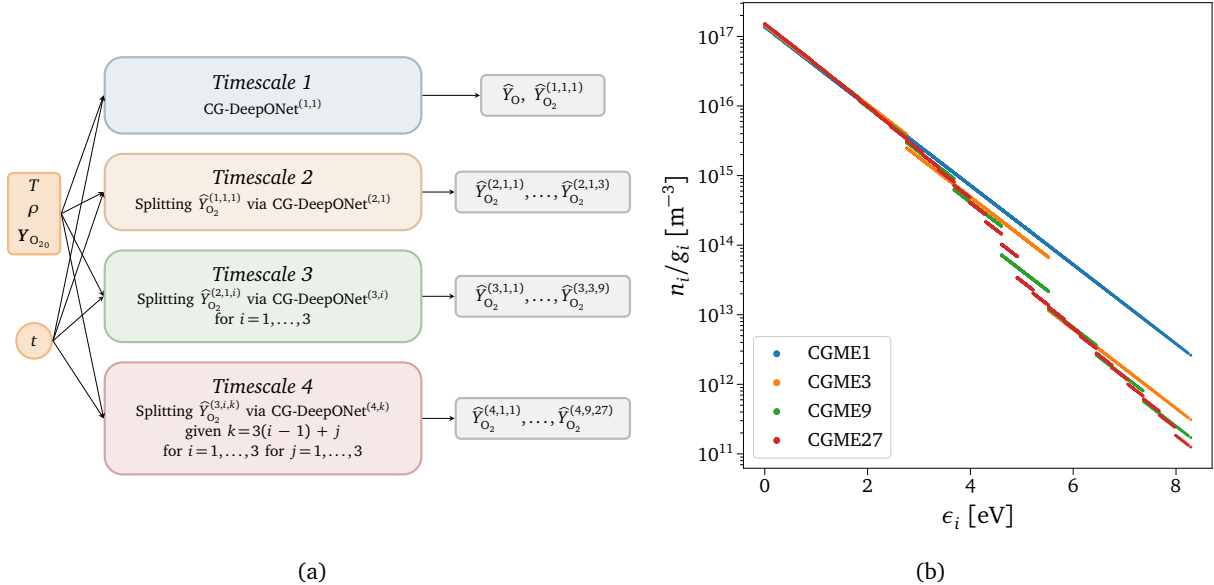


Figure 6. *Hierarchical surrogate for multi-scale coarse-grained dynamics.* (a) Schematics of the complete network architecture. (b) O₂ rovibrational distribution for 1-group (CGME1), 3-groups (CGME3), 9-groups (CGME9), and 27-groups (CGME27) coarse-grained grouping.

2.2.3. Training strategy

Physics-informed neural networks (PINNs) [78] can integrate data and physical governing laws by adding PDE residuals to the loss function of neural networks by relying on automatic differentiation. This capability can also be incorporated into the DeepONet framework (physics-informed DeepONet or PI-DeepONet) [84, 85]. Specifically, the following composite loss function is minimized to train the network parameters, $\boldsymbol{\theta}$:

$$\mathcal{L}(\boldsymbol{\theta}) = \lambda_d \mathcal{L}_d(\boldsymbol{\theta}) + \lambda_r \mathcal{L}_r(\boldsymbol{\theta}) + \lambda_{ic} \mathcal{L}_{ic}(\boldsymbol{\theta}) + \Lambda(\boldsymbol{\theta}), \quad (7)$$

where $\mathcal{L}_d(\boldsymbol{\theta})$ is computed based on the discrepancy between predicted and given data points, $\mathcal{L}_r(\boldsymbol{\theta})$ is the residual loss, $\mathcal{L}_{ic}(\boldsymbol{\theta})$ is the loss over the initial conditions of the 0-D reactor, and $\Lambda(\boldsymbol{\theta})$ contains the L^1 and L^2 regularization

loss. These terms can be expressed as follows:

$$\mathcal{L}_d(\boldsymbol{\theta}) = \frac{1}{N_d} \sum_{i=1}^{N_d} \ell(Y(\mathbf{u}_d^i, t_d^i), \widehat{Y}(\mathbf{u}_d^i, t_d^i)) \quad , \quad (8)$$

$$\mathcal{L}_r(\boldsymbol{\theta}) = \frac{1}{N_r} \sum_{i=1}^{N_r} \mathcal{R}(t_r^i, \rho_r^i, \widehat{Y}(\mathbf{u}_r^i, t_r^i), T_r^i) \quad , \quad (9)$$

$$\mathcal{L}_{ic}(\boldsymbol{\theta}) = \frac{1}{N_{ic}} \sum_{i=1}^{N_{ic}} \ell(Y(\mathbf{u}_{ic}^i, 0), \widehat{Y}(\mathbf{u}_{ic}^i, 0)) \quad , \quad (10)$$

where N_d , N_r , and N_{ic} denote the batch sizes of the training data. Y are the exact mass fraction values from direct numerical simulation of the CG master equations (CGME), whereas \widehat{Y} are the predicted ones from the surrogate. The parameters λ_d , λ_r , and λ_{ic} correspond to weight coefficients in the loss function that can effectively assign a different learning rate to each loss term. In this study, the error function ℓ is expressed as follows:

$$\ell(Y, \widehat{Y}) = \frac{1}{|Y|} \left\| \frac{\ln(Y) - \ln(\widehat{Y})}{\ln(Y)} \right\|_1 \quad , \quad (11)$$

while the residual $\mathcal{R} \in \mathbb{R}$ is

$$\mathcal{R}(t, \rho, \widehat{Y}, T) = \frac{1}{|\widehat{Y}|} \left\| \rho \frac{d\widehat{Y}}{dt} - \Omega^0(\rho, \widehat{Y}, T) \right\|_1 \quad , \quad (12)$$

with Ω^0 being the right hand side of Eq. (3).

Given the hierarchical structure of the proposed surrogate model, the parameters of the entire network are trained by adopting a multi-step procedure:

1. Train sequentially from the slowest to the fastest timescale with only anchor and ICs points ($\lambda_d = 1$, $\lambda_r = 0$, $\lambda_{ic} = 1$) obtained from the numerical solution of the coarse-grained master equations with 1-group, 3-groups, 9-groups, and 27-groups. At each training step, the information acquired is used as a prior for the next one by using fine-tuning transfer learning with L^1 -SP and L^2 -SP regularization as described in Ref. [106].
2. Refine the entire pre-trained model with the complete loss formulation [see Eq. (7)] and weights coefficients λ automatically tuned with the learning rate annealing technique described in Ref. [107].

The choice of employing the residual loss only at the last step is to speed up the training of the entire surrogate.

2.3. Adaptive modeling

Flow simulations are often characterized by regions of strong and weak non-equilibrium conditions of the gas. When the extent of non-equilibrium is large, the highest resolution is needed to resolve all the physical processes accurately. However, there are conditions for which the fine scales (or micro-groups) corresponding to the highest resolution CG model are in equilibrium with other neighboring groups or states. For these cases, the addition of resolution penalizes the computational efficiency rather than improving the model's accuracy. In fact, under these conditions, the population distribution can be approximated with a Boltzmann distribution, and the low-fidelity CG model can accurately resolve their dynamics. Fig. 7 exemplifies what has just been described, as all the reconstructed low-lying energy states from the various CG models can be considered in equilibrium with each other. For this reason, it is sufficient to predict the value of the first CGME3-group, without having to resolve all the timescales. These observations indicate the need to introduce a controller in the algorithm that accurately determines the resolution level needed to describe the dynamics without explicitly computing unnecessary fine scales.

First, defining a metric that can quantify the physical information lost due to the coarse-graining procedure is crucial. This work employs the Euclidean distance between the Boltzmann reconstructed states of the highest resolution CG model (*Timescale 4*) and the remaining low-fidelity ones. Since only the zeroth-order moment of the master equations is considered, the bin-specific coefficient α in Eq. (2) is selected to construct our metric, which can be expressed as follows:

$$\delta^{(ts, \cdot, P)} = \frac{1}{\mathcal{N}_P} \sum_{p, \mathcal{A}^{(4, p)} \subset \mathcal{A}^{(ts, P)}} (\alpha^{(ts, \cdot, P)} - \alpha^{(4, \cdot, p)})^2 \quad , \quad (13)$$

where ts and P (or p) refer to the timescale and its specific group, respectively. Eq. (13) involves the computation of the difference between the offsets (zeroth-order terms), α , of the log-linear Boltzmann distribution functions

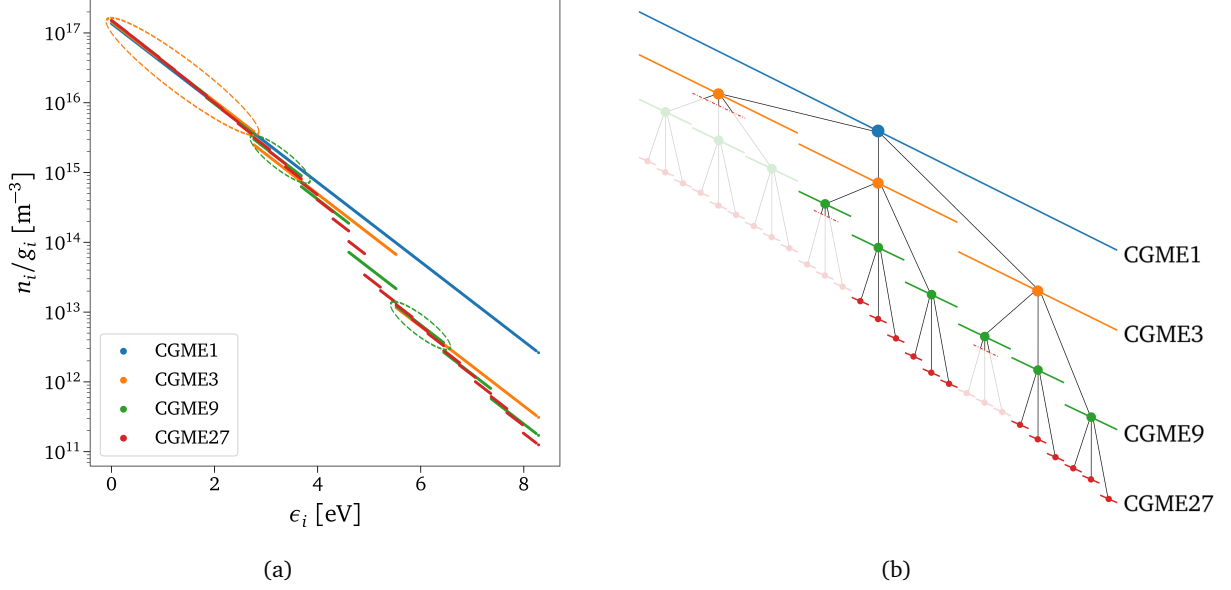


Figure 7. *Example of the adaptation strategy.* (a) O_2 QSS rovibrational distribution for 1-group (CGME1), 3-group (CGME3), 9-group (CGME9), and 27-group (CGME27) coarse-graining. The dashed ovals identify those CG high-resolution groups that can be accurately reconstructed from the low-resolution ones. (b) Exploded view of the groups' graph. The opaque dots represent the Boltzmann-reconstructed groups that correspond to the ovals in (a) and do not require evaluations of CG-DeepONets' high-resolution components.

described in Eq. (2). The sum in Eq. (13) is performed over all the \mathcal{N}_p micro-groups of *Timescale 4* that belong to the macro-group P of timescale ts . Fig. 8(b) provides a visual intuition of Eq. (13) for the first CGME3-group, which consists of the sum of the drawn dashed black lines. We briefly mention that other options for constructing the metric could have relied on the Kullback-Leibler divergence computed between population or energy distributions at the different temporal scales. Given the defined metric, a specific architecture for the non-equilibrium

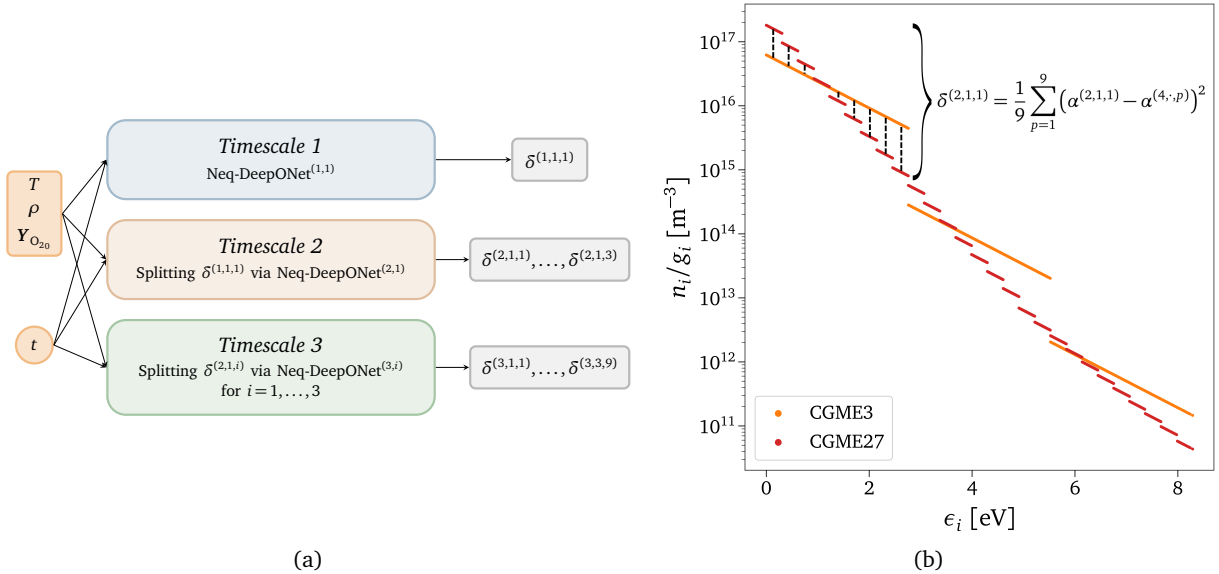


Figure 8. *Adaptive technique.* (a) Schematics of the multi-scale network architecture of the controller responsible for adapting the required coarse-grained model resolution based on the local flow conditions. (b) Euclidean distance metric, δ , used to quantify the physical information lost due to the equilibrium assumption imposed in a too-large subspace in the energy phase. α represents the zeroth-order term, *i.e.*, the offset of the log-linear Boltzmann distribution function defined in Eq. (2).

controller-like surrogate has to be designed. To be consistent with the coarse-grained operator network described in Sec. 2.2.2, we again leverage the multi-scale connotation of the physical problem by separately modeling the underpredicted non-equilibrium values for each CG low-fidelity model, as shown in Fig. 8(a). The outputs of the surrogate are linearly transformed, and a single DeepONet is used for each triplet of values, similar to what has been done for the CG-DeepONets (see Sec. S.3 of the Supplementary Materials for more details).

In summary, the proposed framework combines rovibrational coarse-grained deep operator networks (CG-DeepONets) with non-equilibrium controller DeepONets (Neq-DeepONets). This composition allows the development of a technique that, given an IC and a time instant, adaptively predicts the groups’ distribution with the highest accuracy and lowest computational cost possible. This technique is designed to firstly predict the level of resolution needed given a specific tolerance δ_{tol} , which is sequentially compared (from the slowest to the fastest timescale) with the Neq-DeepONets outputs. If the tolerance is higher than the predicted value, the resolution level is assumed to be sufficient to represent the reactor dynamics. At this point, we highlight the twofold advantage of CG-DeepONets’ hierarchical structure. In fact, other than simplifying the training stage, the presence of the controller boosts the inference phase, as the surrogate relies only on the CG-DeepONets’ components that are truly required to characterize the non-equilibrium distributions. The details of the adaptive algorithm technique are presented in Sec. S.3 of the Supplementary Materials.

3. Results

The framework discussed in the previous sections is used to construct a surrogate model for a 0-D ideal chemical reactor. The first part of the section provides the details of the training and testing of the surrogate, demonstrating its ability to learn the differential operator governing the physics of the reactor. For this purpose, the predictions of the surrogate model are compared against the solution delivered by the numerical integration of the governing equations: the time-resolved distribution and its moments, densities, and energies are the observables used. Details on the adaptivity of the coarse-grained strategy are provided at the end of the section.

3.1. Inference

As explained in Sec. 2.1.2, different initial conditions have been uniformly sampled from Tab. 1 to train and test the proposed ML framework. Fig. 9 shows the broad ranges of the space of ICs for pressure, P_0 , the molar fraction of atomic oxygen, X_{O_0} , and internal temperature, T_{int_0} . A fourth dimension should be considered since the translational temperature of the reactor, T , also varies. In Fig. 9, the red dots represent unseen test scenarios, whereas the black crosses represent the training points.

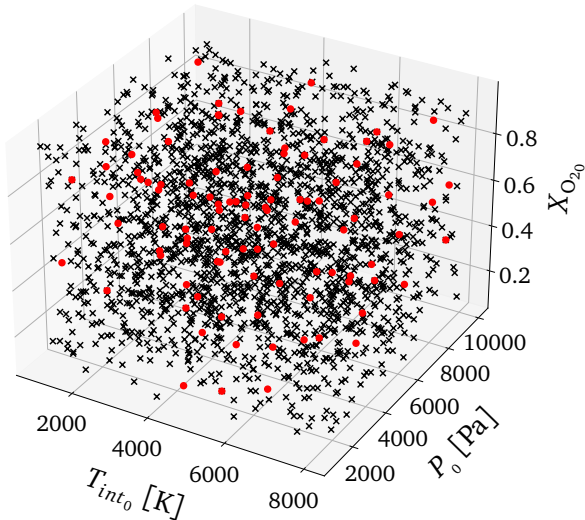


Figure 9. *Space of initial conditions.* The black crosses represent the set of training points, while the red dots identify the testing data set. Note: the figure is missing the last fourth dimension in the space of initial conditions (*i.e.*, the translational temperature of the reactor, T).

Fig. 10(a) compares the exact solution computed by the numerical integrator and the surrogate’s predictions for one unseen scenario taken from the test data set in Fig. 9. The isolated blue line represents the evolution

of the atomic oxygen taken from *Timescale 1*. In contrast, the others describe the dynamics of the 27 rovibrational energy-based groups predicted by *Timescale 4*. The inference has been performed by interrogating the CG-DeepONet based on the vector of time instants generated from the numerical integrator and the given initial conditions, defined by $\{[T, \rho, Y_{O_{20}}], t_k\}_{k=1}^M$, with M the number of evaluation points. From Fig. 10(a), an excel-

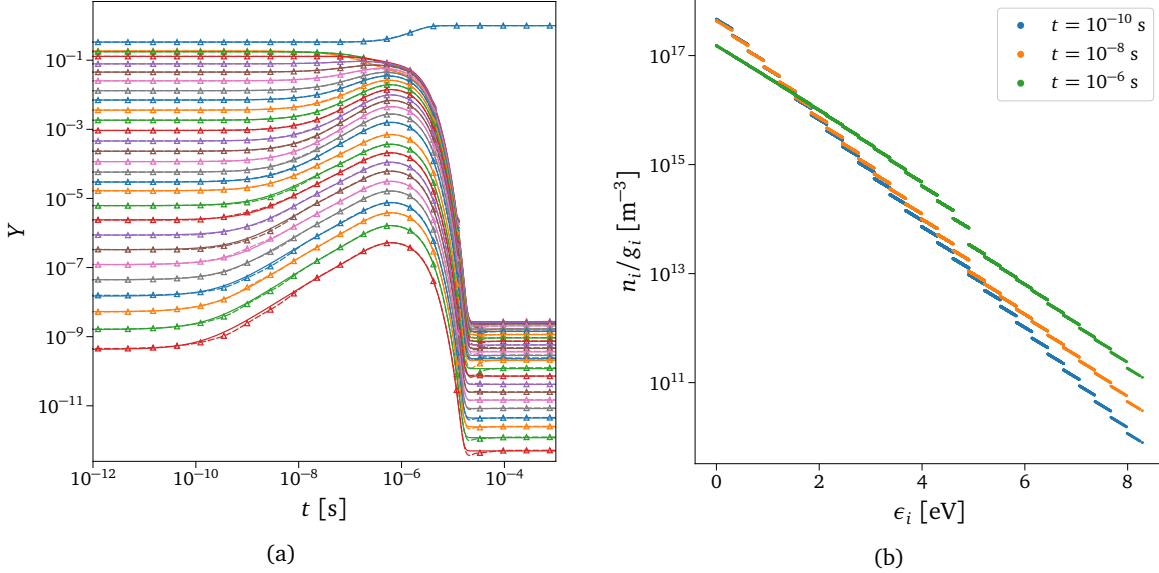


Figure 10. *Inferred solution*. (a) Reference solution (solid line) versus prediction from the trained model (dashed line with markers). The isolated blue line represents the evolution of the atomic oxygen, while the remaining are the 27 groups of O_2 in ascending order of energy content per particle (top-down). Initial conditions used: $P_0 = 3617.24$ Pa, $X_{O_0} = 0.4996$, $T_{int_0} = 4333.16$ K, $T = 9742.13$ K. (b) Predicted O_2 rovibrational states distribution at three different time instants taken from the dynamics shown in (a).

lent agreement between the predicted and the exact solution can be observed. We can conclude that the trained model can yield accurate predictions for different and unseen initial conditions (see Sec. S.2.2 in the Supplementary Materials for additional test cases). Negligible discrepancies can be noticed in various regions of the dynamics of the heat bath, which can be improved by further refining the trained model. To the author’s best knowledge, this work provides the first application of the PI-DeepONets to a dynamical system containing many such degrees of freedom. The main reason for such good surrogation of the dynamics is that the hierarchical structure of the proposed deep learning framework embodies the physical connotations of the problem. The micro-groups inside each macro-groups equilibrate faster between each other than with other ones outside it. For this reason, they show very similar behavior in their dynamics, which can be captured by the few modes discovered by the shared trunk. This aspect facilitates reaching high levels of accuracy with a relatively small number of network parameters. Indeed, the surrogate correctly predicts the dynamics of almost thirty species spanning a wide range of orders of magnitude (around 12) in mass fractions values. Additionally, to expand the initial conditions’ space even further by keeping such a high accuracy level and relatively small network architecture, one could consider constructing multiple surrogates. Each of these surrogates can be built with the same architecture but specialized for a local sub-domain in the space of the initial conditions.

3.2. Accuracy

The relative L^2 -norm has been used as the error metric to evaluate the accuracy of the surrogate model, consistently with Ref. [84]. In particular, the employed test error corresponds to the mean relative error of the surrogate’s predictions for *Timescale 4* over all the examples in the test data set:

$$\epsilon^{(j)} = \frac{1}{N} \sum_{i=1}^N \frac{\left\| \widehat{Y}_i^{(4,;j)}(t) - Y_i^{(4,;j)}(t) \right\|_2}{\left\| Y_i^{(4,;j)}(t) \right\|_2} \quad \text{for } j \in \{1, \dots, \mathcal{N}_g\}, \quad (14)$$

where $\mathcal{N}_g = 27$ is the number of groups, $N = 100$ denotes the number of testing cases, and t is a set of log-uniformly spaced points in the time domain. To perform this analysis, 1 000 points in time have been sampled

from each testing scenario to perform this analysis. The four highest errors of the inferred solution are presented in Tab. 2. Once again, the reported values confirm the excellent agreement between the numerically integrated master equations and the predicted solutions, as the maximum relative L^2 -norm error is less than 4%.

Group	Rel. error [%]
$\widehat{Y}^{(4,3,9)}$	3.34 ± 2.55
$\widehat{Y}^{(4,9,27)}$	3.29 ± 1.70
$\widehat{Y}^{(4,6,17)}$	3.18 ± 2.45
$\widehat{Y}^{(4,9,26)}$	3.10 ± 1.72

Table 2. *Test error.* The four highest mean relative L^2 -norm testing errors (with standard deviations) of the trained model for *Timescale 4*.

3.3. Coarse-grained surrogate compared to numerically-integrated StS master equations and Park’s model

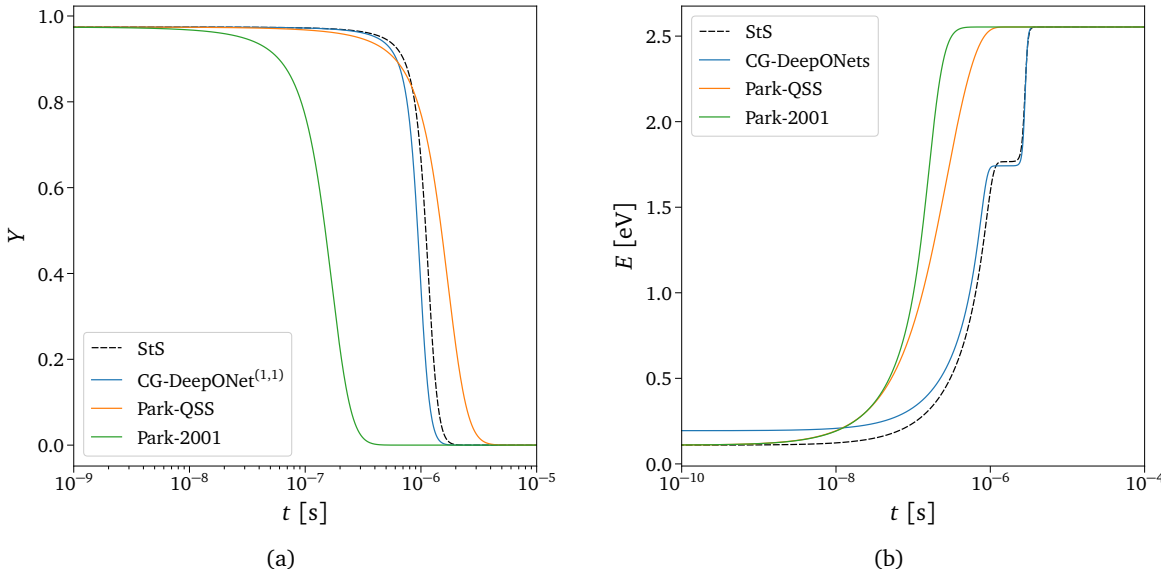


Figure 11. *Coarse-grained surrogate vs. StS master equations vs. Park’s model.* The black dashed line represents the state-to-state solution, the blue line the predicted coarse-grained surrogate, and the orange and green lines the Park’s two-temperature model solution with the QSS approach [5] and the kinetics from Ref. [108], respectively. Initial conditions used: $P_0 = 1\,000$ Pa, $X_{O_2} = 0.05$, $T_{int_0} = 1\,000$ K, $T = 15\,000$ K. (a) Evolution of total mass fraction of O_2 . (b) Weighted rovibrational energy evolution per particle of O_2 .

To demonstrate the level of physical accuracy of the coarse-grained surrogate discussed here, the results provided by the surrogate are compared against the high-fidelity state-to-state solution and the less accurate but computationally cheap two-temperature model of Park, which is a particular case of the multi-temperature models described in 2.1. Both StS and Park’s solutions have been computed with traditional numerical integrators. In Fig. 11(a), two different approaches are considered for Park’s model, one employing the less accurate but still widely used kinetics from Ref. [108], derived from empirical methods or experimental data, and the other using the more recent QSS approach [5], whose kinetic database is directly computed from state-to-state calculations. Fig. 11(a) shows the evolution of the total mass fraction of O_2 for the different models considered. It is evident from the figure that the closest solution to state-to-state modeling is the coarse-grained grouping strategy employed in this work. Only *Timescale 1* (or CG-DeepONet^(1,1)) of the proposed surrogate model has been interogated to produce the results shown in Fig. 11(a). This is because it implicitly contains all the information about the energy transfer processes between the 27 groups, as it has been trained with the O_2 data from the integration

of CGME27. Therefore, if only *Timescale 1* is used to predict the dynamics of the total mass fraction of the reactor species, the solution can be more accurate than any two-temperature model. However, CG-DeepONet^(1,1) is not sufficient to accurately predict the total internal energy content of the molecule since the proposed surrogate is designed to model only the zeroth-order moment of the master equations. Therefore, this quantity generally requires the evaluation of the overall surrogate, which includes the low-scale components CG-DeepONet^(2:4,:). The discrepancy between the CG surrogate’s predictions and the StS numerical solution in Fig. 11 is almost exclusively determined by the physical simplifications made by the CG model. In particular, the energy difference that can be noticed at the initial time instants is caused by the fact that the reconstructed states within each bin follow a Boltzmann distribution at the translational temperature T (for the assumptions made in Sec. 2.1.2). In contrast, the quantum energy levels for the StS solution follow a distribution at temperature T_{int_0} .

One could upgrade the proposed hierarchical architecture to model also higher-order moments of the master equations. For example, the same architecture as the CG-DeepONets one should be replicated to model the internal energy content of every single bin. Consequently, CG-DeepONet^(1,1) could correctly predict both zeroth-, *i.e.*, total mass, and first-order moment, *i.e.*, internal energy, of O₂. In such a case, the low-scale components CG-DeepONet^(2:4,:) would not be required to predict the solution shown in Fig. 11(b), but they might still be necessary in providing the correct distribution function of the quantum energy states when considering other physical phenomena, such as radiation.

3.4. Adaptive technique

The advantage of the hierarchical architecture proposed in this work is the ability to tailor the model complexity to the specific localized flow conditions to obtain a computationally efficient yet accurate physical model. Fig. 12

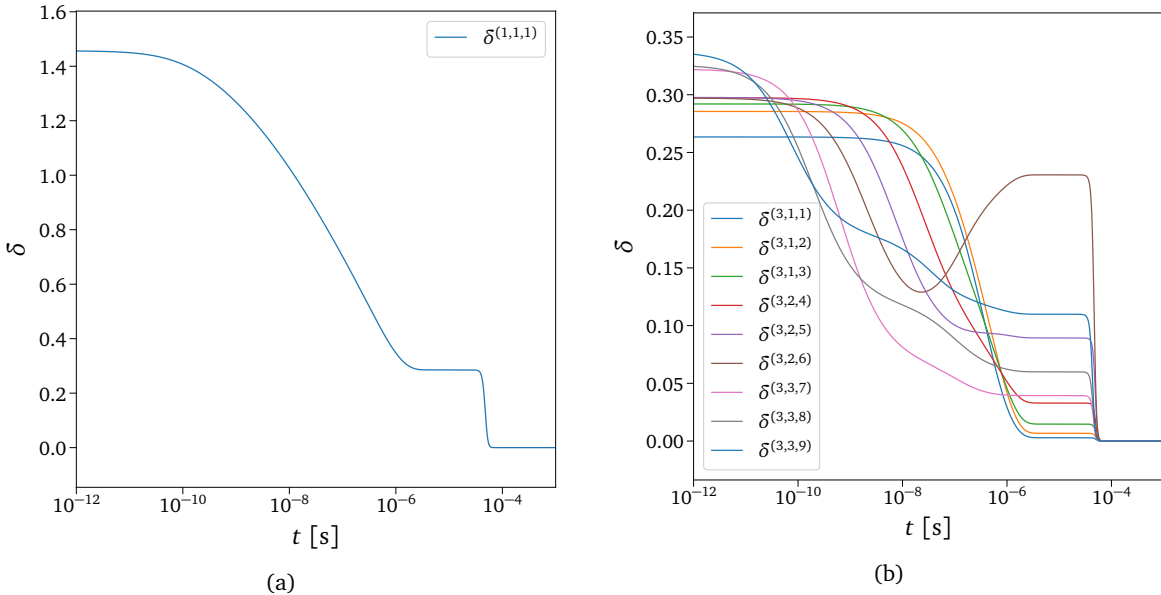


Figure 12. *Underpredicted non-equilibrium metrics.* Dynamics of underpredicted non-equilibrium metrics evaluated by reconstructing the 27 groups with predictions from *Timescale 1* (a) and *Timescale 3* (b) for the same test case shown in Fig. 13.

shows an example of the dynamics of underpredicted non-equilibrium Euclidean metric computed via Eq. (13) for *Timescale 1* (Fig. 12(a)), and *Timescale 3* (Fig. 12(b)) for the same test case shown in Fig. 13. The values plotted in Fig. 12 can be considered a good reference for the space the proposed metric can span, as the analyzed test case is characterized by a high initial thermal and chemical non-equilibrium. It should be noted that the values of $\delta^{(1,1,1)}$ reported in Fig. 12(a) are almost an order of magnitude larger than Fig. 12(b) due to the more accurate modeling adopted in the latter. Overall, the trend is decreasing by approaching the equilibrium, except for the evident QSS region starting around 10^{-6} s, where all the quantities remain constant. $\delta^{(3,2,6)}$ shows an interesting behavior in Fig. 12(b), which corresponds to the sixth group of the 9-groups rovibrational energy-based coarse-grained grouping strategy for *Timescale 3*, the one close to the dissociation energy (5.115 eV). By observing the highly non-equilibrium StS dynamics at QSS of the states in this group (*e.g.*, Fig. 2), it is clear that the highest resolution possible is necessary for that region of the energy space to model the dynamics of those states accurately [5].

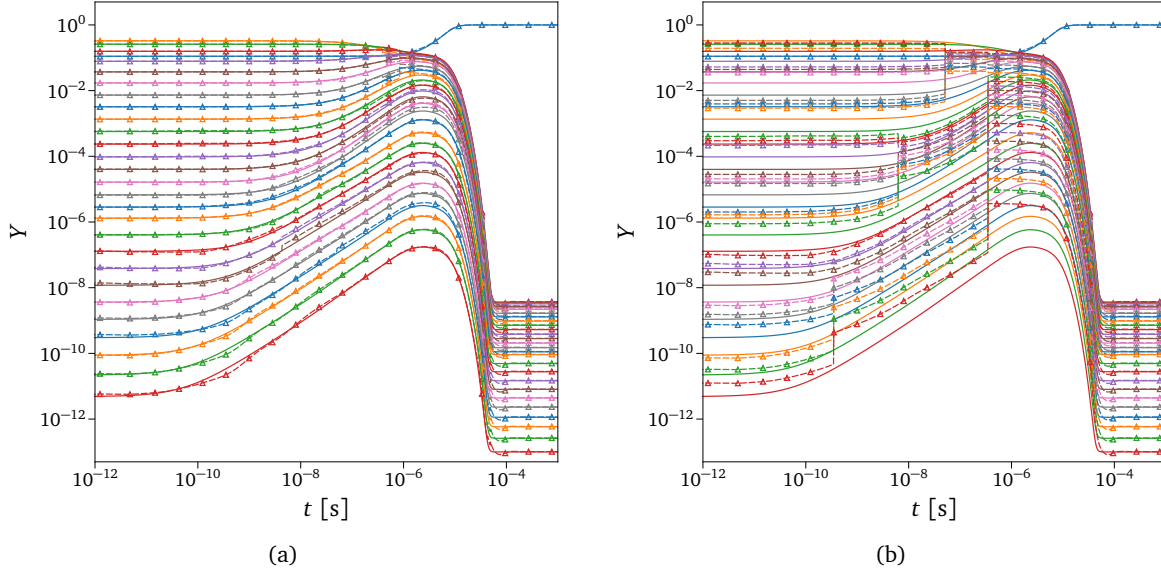


Figure 13. *Exact vs. adaptive solution for different δ_{tol} .* (a) Underpredicted non-equilibrium tolerance: $\delta_{tol} = 0.1$. (b) Underpredicted non-equilibrium tolerance: $\delta_{tol} = 0.5$. Exact solution (solid line) versus prediction from the trained surrogate (dashed line with markers) using the adaptive technique shown in Sec. 2.3. The isolated blue line represents the evolution of the atomic oxygen, while the remaining are the 27 groups of O_2 in ascending order of energy content per particle (top-down). Initial conditions used: $P_0 = 3000$ Pa, $X_{O_2} = 0.2$, $T_{int_0} = 3500$ K, $T = 15000$ K.

The solution obtained with the adaptive technique is compared with the exact one in Fig. 13 for two different values of the underpredicted non-equilibrium metric tolerance, δ_{tol} . This value acts as a discriminant for assuming equilibrium inside each macro-group for all the timescales modeled. For $\delta_{tol} = 0.1$, the adaptation starts playing effect just before the QSS region, as can also be deduced from Fig. 12(b), whereas for $\delta_{tol} = 0.5$, it already acts at the beginning of the dynamics. We can assert that for a value of $\delta_{tol} = 0.1$, the solution looks very similar to the exact one, supporting the effectiveness of the adaptive technique in terms of physical accuracy. The adaptive solutions shown in Fig. 13 have been obtained by solving the number of groups dictated by the respective δ reported in Fig. 14(c) as functions of time. From Fig. 14(c), it is evident that the number of the solved groups decreases considerably by increasing the tolerance value, confirming the validity of the proposed adaptive technique. The prediction of the total mass fraction of O_2 shown in Fig. 14(a) is independent of the tolerance used since our model has been trained such that even the low-fidelity coarse-grained models can correctly predict the actual mass of the reactor species. In the case of energy, the choice of the proper tolerance can play an essential role in predicting its correct value, as shown in Fig. 14(b).

Fig. 14(d) presents a preliminary performance analysis of the adaptive technique for the different tolerance values based on a comparison with the standalone CG-DeepONet model. The reported timings are obtained as the mean of 1000 different inference evaluations of the model per each physical time instant, conducted with a single central processing unit (CPU) core (Intel® Xeon® Processor E3-1285 v6). All these computations have been performed in the TensorFlow [109] environment, which means that a large part of the network evaluation time involves Python call overhead. The bar plot shows that the adaptive technique outperforms the standalone surrogate later in the system’s dynamical evolution when the composition approaches the asymptotic equilibrium value. The opaque bar chunks in Fig. 14(d) represent the contribution to the inference cost due to the Neq-DeepONets surrogate. The reported timings should also be considered from the perspective of CFD. For example, one could consider the cell values in a multi-dimensional mesh for hypersonic simulation as the input data for the surrogate model. Most of these cells will lay in the equilibrium or near-equilibrium domain, while the few remaining ones will be in a strong non-equilibrium region (e.g., shock proximity). In light of these considerations and the performances shown in Fig. 14(d), we can reasonably assert that using the adaptive technique has the potential to outperform the standalone model in a multi-dimensional simulation framework. Another great advantage of this methodology is its flexibility, as computational costs and physical accuracy can be easily balanced by tuning the tolerance value, δ_{tol} . Moreover, inference with physics-informed DeepONets is trivially parallelizable with graphics processing units (GPUs), which can remarkably boost the inference timings shown in Fig. 14(d). Wang

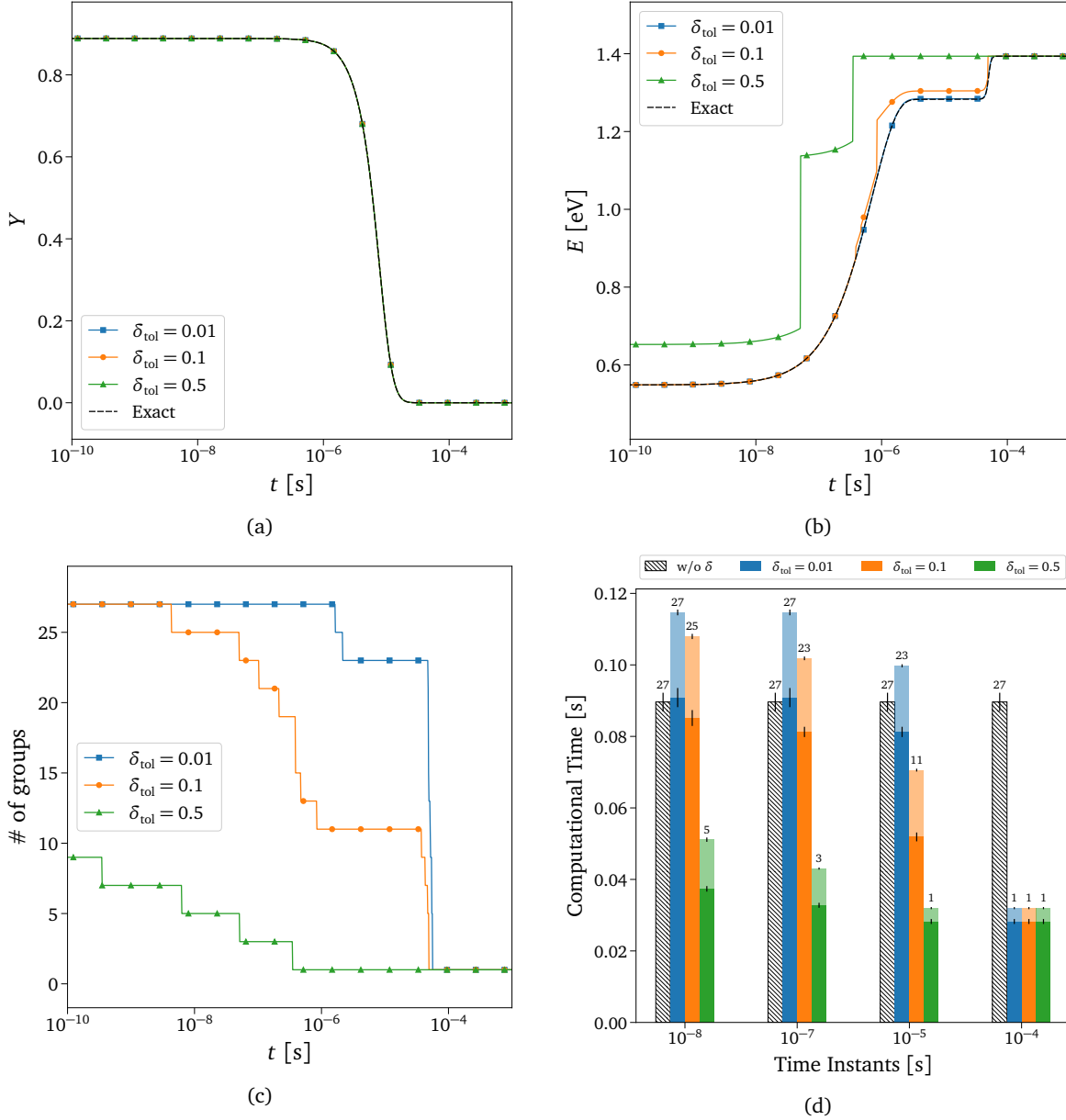


Figure 14. Adaptive solution for different values of underpredicted non-equilibrium tolerance. (a) Total mass fraction evolution of O_2 . (b) Weighted sum of the grouped-specific O_2 rovibrational energy, with weights given by the groups' distribution. (c) Total number of actually modeled O_2 groups. (d) Computational cost comparison between the adaptive technique and the standalone CG-DeepONet model for single-time instant evaluation. The numbers on top of the bars are the corresponding number of groups, also shown in (c).

et al. [84] have already demonstrated that the PI-DeepONets can outperform and replace conventional numerical solvers for long-time integration [85].

4. Conclusions

We proposed a new machine learning-based paradigm inspired and constrained by physical laws for solving multi-scale non-equilibrium flows. The designed model (CG-DeepONet) sequentially learned the integral solution operator for multi-fidelity coarse-grained master equations by employing a physics-inspired hierarchical architecture, where physics-informed DeepONet (PI-DeepONet) represents the core element. Furthermore, we developed a

controller-like surrogate (Neq-DeepONet) to learn the dynamics of the underpredicted degree of non-equilibrium to tailor the model's accuracy to the local non-equilibrium conditions. Combining the two, we designed a novel adaptive predictive technique for non-equilibrium thermochemical processes, which showed flexibility in balancing accuracy and computational cost. The CG-DeepONet surrogate alone exhibited excellent physical accuracy compared to the direct numerical simulations, with a relative error smaller than 4%, and good computational efficiency when the adaptive method is used, gaining more than 3X speedup close to the asymptotic equilibrium.

In this work, the proposed methodology has been applied to the study of chemical kinetics relevant for application to hypersonic flight and has been tested on oxygen mixtures. However, the framework is not constrained to the chosen thermochemical configuration, but it can be extended to adiabatic Air-5 mixtures (*i.e.*, simultaneously with N₂, O₂, NO, N, and O species) or even other fields of physics spanning a wide range of temporal scales, such as electromagnetism, magnetohydrodynamics, and more generally, plasma physics. The hierarchical surrogate model has the potential to remove the stiffness-associated source terms in reacting flow simulations by coupling it with a Navier-Stokes solver through operator-splitting techniques (*e.g.*, Strang splitting [110]). From the CFD perspective, the surrogate could be used in two different ways:

- To adaptively describe the internal quantum states distribution by combining the CG-DeepONet predictive capabilities with the Neq-DeepONet regulative ones. This choice is necessary when the distribution function is needed, for example, with radiative phenomena considered;
- To provide macroscopic quantities such as total mass fraction or total internal energy content (if modeled) by interrogating only *Timescale 1* of the proposed architecture.

Future work will address the coupling and testing of the proposed surrogate with Navier-Stokes solvers for high-speed flow numerical simulations.

Acknowledgements

The work is supported by the Vannevar Bush Faculty Fellowship OUSD(RE) Grant No: N00014-21-1-295 with Prof. Marco Panesi as the Principal Investigator. The authors wish to thank Dr. Pietro Novelli (Istituto Italiano di Tecnologia, Italy) for many helpful discussions. The views and conclusions contained herein are those of the authors and should not be interpreted as necessarily representing the official policies or endorsements, either expressed or implied, of the U.S. government.

References

- [1] P. A. Gnoffo. "PLANETARY-ENTRY GAS DYNAMICS". In: *Annual Review of Fluid Mechanics* 31.1 (Jan. 1999), pp. 459–494. DOI: 10.1146/annurev.fluid.31.1.459.
- [2] C. O. Johnston and M. Panesi. "Impact of state-specific flowfield modeling on atomic nitrogen radiation". In: *Physical Review Fluids* 3.1 (Jan. 2018), p. 013402. DOI: 10.1103/PhysRevFluids.3.013402.
- [3] A. Harpale, M. Panesi, and H. B. Chew. "Communication: Surface-to-bulk diffusion of isolated versus interacting C atoms in Ni(111) and Cu(111) substrates: A first principle investigation". In: *The Journal of Chemical Physics* 142.6 (Feb. 2015), p. 061101. DOI: 10.1063/1.4907716.
- [4] A. Harpale, M. Panesi, and H. B. Chew. "Plasma-graphene interaction and its effects on nanoscale patterning". In: *Physical Review B* 93.3 (Jan. 2016), p. 035416. DOI: 10.1103/PhysRevB.93.035416.
- [5] M. Panesi et al. "Rovibrational internal energy transfer and dissociation of N₂(¹Σ_g⁺)-N(⁴S_u) system in hypersonic flows". In: *The Journal of Chemical Physics* 138.4 (Jan. 2013), p. 044312. DOI: 10.1063/1.4774412.
- [6] M. Panesi et al. "Nonequilibrium shock-heated nitrogen flows using a rovibrational state-to-state method". In: *Physical Review E* 90.1 (July 2014), p. 013009. DOI: 10.1103/PhysRevE.90.013009.
- [7] A. Munafò et al. "Modeling of non-equilibrium phenomena in expanding flows by means of a collisional-radiative model". In: *Physics of Plasmas* 20.7 (July 2013), p. 073501. DOI: 10.1063/1.4810787.
- [8] E. Kustova and M. Mekhonoshina. "Models for bulk viscosity in carbon dioxide". In: *AIP Conference Proceedings* 2132.1 (2019), p. 150006. DOI: 10.1063/1.5119646.
- [9] E. A. Nagnibeda and E. Kustova. *Non-Equilibrium Reacting Gas Flows*. Heat and Mass Transfer. Berlin, Heidelberg: Springer Berlin Heidelberg, 2009. DOI: 10.1007/978-3-642-01390-4.
- [10] M. Panesi et al. "Electronic Excitation of Atoms and Molecules for the FIRE II Flight Experiment". In: *Journal of Thermophysics and Heat Transfer* 25.3 (July 2011), pp. 361–374. DOI: 10.2514/1.50033.
- [11] R. L. Macdonald et al. "Nonequilibrium radiation and dissociation of CO molecules in shock-heated flows". In: *Physical Review Fluids* 1.4 (Aug. 2016), p. 043401. DOI: 10.1103/PhysRevFluids.1.043401.

- [12] M. Capitelli et al. *Fundamental Aspects of Plasma Chemical Physics*. Vol. 85. Springer Series on Atomic, Optical, and Plasma Physics. New York, NY: Springer New York, 2016. DOI: 10.1007/978-1-4419-8185-1.
- [13] R. L. Macdonald et al. “State-to-State Master Equation and Direct Molecular Simulation Study of Energy Transfer and Dissociation for the N_2 -N System”. In: *The Journal of Physical Chemistry A* 124.35 (Sept. 2020), pp. 6986–7000. DOI: 10.1021/acs.jpca.0c04029.
- [14] D. Wang et al. “Quantal study of the exchange reaction for $N+N_2$ using an ab initio potential energy surface”. In: *The Journal of Chemical Physics* 118.5 (Feb. 2003), pp. 2186–2189. DOI: 10.1063/1.1534092.
- [15] F. Esposito, I. Armenise, and M. Capitelli. “N- N_2 state to state vibrational-relaxation and dissociation rates based on quasiclassical calculations”. In: *Chemical Physics* 331.1 (Dec. 2006), pp. 1–8. DOI: 10.1016/j.chemphys.2006.09.035.
- [16] B. R. L. Galvão and A. J. C. Varandas. “Accurate Double Many-Body Expansion Potential Energy Surface for $N_3(^4A)$ from Correlation Scaled ab Initio Energies with Extrapolation to the Complete Basis Set Limit”. In: *The Journal of Physical Chemistry A* 113.52 (Dec. 2009), pp. 14424–14430. DOI: 10.1021/jp903719h.
- [17] R. L. Jaffe, D. W. Schwenke, and G. Chaban. “Theoretical Analysis of N_2 Collisional Dissociation and Rotation-Vibration Energy Transfer”. In: *47th AIAA Aerospace Sciences Meeting including The New Horizons Forum and Aerospace Exposition*. Reston, Virginia: American Institute of Aeronautics and Astronautics, Jan. 2009. DOI: 10.2514/6.2009-1569.
- [18] S. Venturi, R. L. Jaffe, and M. Panesi. “Bayesian Machine Learning Approach to the Quantification of Uncertainties on Ab Initio Potential Energy Surfaces”. In: *The Journal of Physical Chemistry A* 124.25 (June 2020), pp. 5129–5146. DOI: 10.1021/acs.jpca.0c02395.
- [19] P. Hammerling, J. D. Teare, and B. Kivel. “Theory of Radiation from Luminous Shock Waves in Nitrogen”. In: *Physics of Fluids* 2.4 (1959), p. 422. DOI: 10.1063/1.1724413.
- [20] O. Knab, H.-H. Fruehauf, and E. W. Messerschmid. “Theory and validation of the physically consistent coupled vibration-chemistry-vibration model”. In: *Journal of Thermophysics and Heat Transfer* 9.2 (Apr. 1995), pp. 219–226. DOI: 10.2514/3.649.
- [21] Y. Zhu et al. “Physics-constrained deep learning for high-dimensional surrogate modeling and uncertainty quantification without labeled data”. In: *Journal of Computational Physics* 394 (Oct. 2019), pp. 56–81. DOI: 10.1016/j.jcp.2019.05.024.
- [22] E. Haghighat et al. “A physics-informed deep learning framework for inversion and surrogate modeling in solid mechanics”. In: *Computer Methods in Applied Mechanics and Engineering* 379 (June 2021), p. 113741. DOI: 10.1016/j.cma.2021.113741.
- [23] L. Sun et al. “Surrogate modeling for fluid flows based on physics-constrained deep learning without simulation data”. In: *Computer Methods in Applied Mechanics and Engineering* 361 (Apr. 2020), p. 112732. DOI: 10.1016/j.cma.2019.112732.
- [24] Y. Choi et al. “Space-time reduced order model for large-scale linear dynamical systems with application to Boltzmann transport problems”. In: *Journal of Computational Physics* 424 (Jan. 2021), p. 109845. DOI: 10.1016/j.jcp.2020.109845.
- [25] H. You et al. “Data-driven learning of nonlocal physics from high-fidelity synthetic data”. In: *Computer Methods in Applied Mechanics and Engineering* 374 (Feb. 2021), p. 113553. DOI: 10.1016/j.cma.2020.113553.
- [26] C. V. Mai et al. “SURROGATE MODELING FOR STOCHASTIC DYNAMICAL SYSTEMS BY COMBINING NONLINEAR AUTOREGRESSIVE WITH EXOGENOUS INPUT MODELS AND POLYNOMIAL CHAOS EXPANSIONS”. In: *International Journal for Uncertainty Quantification* 6.4 (2016), pp. 313–339. DOI: 10.1615/Int.J.UncertaintyQuantification.2016016603.
- [27] G. Rozza, D. B. P. Huynh, and A. T. Patera. “Reduced Basis Approximation and a Posteriori Error Estimation for Affinely Parametrized Elliptic Coercive Partial Differential Equations”. In: *Archives of Computational Methods in Engineering* 15.3 (Sept. 2008), pp. 229–275. DOI: 10.1007/s11831-008-9019-9.
- [28] P. Benner, S. Gugercin, and K. Willcox. “A Survey of Projection-Based Model Reduction Methods for Parametric Dynamical Systems”. In: *SIAM Review* 57.4 (Jan. 2015), pp. 483–531. DOI: 10.1137/130932715.
- [29] D. Amsallem and C. Farhat. “Stabilization of projection-based reduced-order models”. In: *International Journal for Numerical Methods in Engineering* 91.4 (July 2012), pp. 358–377. DOI: 10.1002/nme.4274.
- [30] C. Huang et al. “Model reduction for multi-scale transport problems using model-form preserving least-squares projections with variable transformation”. In: *Journal of Computational Physics* 448 (Jan. 2022), p. 110742. DOI: 10.1016/j.jcp.2021.110742.

- [31] R. Swischuk et al. “Projection-based model reduction: Formulations for physics-based machine learning”. In: *Computers & Fluids* 179 (Jan. 2019), pp. 704–717. DOI: 10.1016/j.compfluid.2018.07.021.
- [32] Y. Choi and K. Carlberg. “Space-Time Least-Squares Petrov-Galerkin Projection for Nonlinear Model Reduction”. In: *SIAM Journal on Scientific Computing* 41.1 (Jan. 2019), A26–A58. DOI: 10.1137/17M1120531.
- [33] K. Carlberg, C. Bou-Mosleh, and C. Farhat. “Efficient non-linear model reduction via a least-squares Petrov-Galerkin projection and compressive tensor approximations”. In: *International Journal for Numerical Methods in Engineering* 86.2 (Apr. 2011), pp. 155–181. DOI: 10.1002/nme.3050.
- [34] A. I. J. Forrester, A. Sóbester, and A. J. Keane. *Engineering Design via Surrogate Modelling*. Wiley, July 2008, pp. 205–210. DOI: 10.1002/9780470770801.
- [35] J. Xu and K. Duraisamy. “Multi-level convolutional autoencoder networks for parametric prediction of spatio-temporal dynamics”. In: *Computer Methods in Applied Mechanics and Engineering* 372 (Dec. 2020), p. 113379. DOI: 10.1016/j.cma.2020.113379.
- [36] Y. Kim et al. “A fast and accurate physics-informed neural network reduced order model with shallow masked autoencoder”. In: *Journal of Computational Physics* 451 (Feb. 2022), p. 110841. DOI: 10.1016/j.jcp.2021.110841.
- [37] E. Ozbenli et al. “Numerical solution of hypersonic flows via artificial neural networks”. In: *AIAA Scitech 2020 Forum*. Reston, Virginia: American Institute of Aeronautics and Astronautics, Jan. 2020. DOI: 10.2514/6.2020-1233.
- [38] G. Colonna et al. “Reduction of State-to-State Kinetics to Macroscopic Models in Hypersonic Flows”. In: *Journal of Thermophysics and Heat Transfer* 20.3 (July 2006), pp. 477–486. DOI: 10.2514/1.18377.
- [39] L. Campoli, E. Kustova, and P. Maltseva. “Assessment of Machine Learning Methods for State-to-State Approach in Nonequilibrium Flow Simulations”. In: *Mathematics* 10.6 (Mar. 2022), p. 928. DOI: 10.3390/math10060928.
- [40] C. Scherding et al. “Data-driven framework for input/output lookup tables reduction - with application to hypersonic flows in chemical non-equilibrium”. In: (2022). DOI: 10.48550/ARXIV.2210.04269.
- [41] I. Zanardi, S. Venturi, and M. Panesi. “Towards Efficient Simulations of Non-Equilibrium Chemistry in Hypersonic Flows: A Physics-Informed Neural Network Framework”. In: *AIAA SCITECH 2022 Forum*. Reston, Virginia: American Institute of Aeronautics and Astronautics, Jan. 2022. DOI: 10.2514/6.2022-1639.
- [42] M. Panesi and A. Lani. “Collisional radiative coarse-grain model for ionization in air”. In: *Physics of Fluids* 25.5 (May 2013), p. 057101. DOI: 10.1063/1.4804388.
- [43] A. Munafò, M. Panesi, and T. E. Magin. “Boltzmann rovibrational collisional coarse-grained model for internal energy excitation and dissociation in hypersonic flows”. In: *Physical Review E* 89.2 (Feb. 2014), p. 023001. DOI: 10.1103/PhysRevE.89.023001.
- [44] A. Munafò, Y. Liu, and M. Panesi. “Modeling of dissociation and energy transfer in shock-heated nitrogen flows”. In: *Physics of Fluids* 27.12 (Dec. 2015), p. 127101. DOI: 10.1063/1.4935929.
- [45] Y. Liu et al. “General multi-group macroscopic modeling for thermo-chemical non-equilibrium gas mixtures”. In: *The Journal of Chemical Physics* 142.13 (Apr. 2015), p. 134109. DOI: 10.1063/1.4915926.
- [46] A. Sahai et al. “Adaptive coarse graining method for energy transfer and dissociation kinetics of polyatomic species”. In: *The Journal of Chemical Physics* 147.5 (Aug. 2017), p. 054107. DOI: 10.1063/1.4996654.
- [47] N. Kovachki et al. “Neural Operator: Learning Maps Between Function Spaces”. In: (2020). DOI: 10.48550/ARXIV.2108.08481.
- [48] D. P. Kingma and M. Welling. “Auto-Encoding Variational Bayes”. In: (2013). DOI: 10.48550/ARXIV.1312.6114.
- [49] R. R. Coifman et al. “Geometric diffusions as a tool for harmonic analysis and structure definition of data: Diffusion maps”. In: *Proceedings of the National Academy of Sciences* 102.21 (May 2005), pp. 7426–7431. DOI: 10.1073/pnas.0500334102.
- [50] B. Schölkopf, A. Smola, and K.-R. Müller. “Nonlinear Component Analysis as a Kernel Eigenvalue Problem”. In: *Neural Computation* 10.5 (July 1998), pp. 1299–1319. DOI: 10.1162/089976698300017467.
- [51] V. Oommen et al. “Learning two-phase microstructure evolution using neural operators and autoencoder architectures”. In: (2022). DOI: 10.48550/ARXIV.2204.07230.
- [52] B. A. Merchant and J. D. Madura. “A Review of Coarse-Grained Molecular Dynamics Techniques to Access Extended Spatial and Temporal Scales in Biomolecular Simulations”. In: *Annual Reports in Computational Chemistry*. Ed. by R. A. Wheeler. Vol. 7. Annual Reports in Computational Chemistry. Elsevier, 2011, pp. 67–87. DOI: 10.1016/B978-0-444-53835-2.00003-1.

- [53] S. Kmiecik et al. “Coarse-Grained Protein Models and Their Applications”. In: *Chemical Reviews* 116.14 (July 2016), pp. 7898–7936. DOI: 10.1021/acs.chemrev.6b00163.
- [54] M. J. Boniecki et al. “SimRNA: a coarse-grained method for RNA folding simulations and 3D structure prediction”. In: *Nucleic Acids Research* 44.7 (Apr. 2016), e63–e63. DOI: 10.1093/nar/gkv1479.
- [55] K. L. Heritier et al. “Energy transfer models in nitrogen plasmas: Analysis of $N_2(^1\Sigma_g^+)$ - $N(^4S_u)$ - e^- interaction”. In: *The Journal of Chemical Physics* 141.18 (Nov. 2014), p. 184302. DOI: 10.1063/1.4900508.
- [56] F. Esposito, M. Capitelli, and C. Gorse. “Quasi-classical dynamics and vibrational kinetics of $N+N_2(v)$ system”. In: *Chemical Physics* 257.2-3 (July 2000), pp. 193–202. DOI: 10.1016/S0301-0104(00)00155-5.
- [57] S. Venturi et al. “Data-Inspired and Physics-Driven Model Reduction for Dissociation: Application to the O_2+O System”. In: *The Journal of Physical Chemistry A* 124.41 (Oct. 2020), pp. 8359–8372. DOI: 10.1021/acs.jpca.0c04516.
- [58] M. Sharma Priyadarshini, Y. Liu, and M. Panesi. “Coarse-grained modeling of thermochemical nonequilibrium using the multigroup maximum entropy quadratic formulation”. In: *Physical Review E* 101.1 (Jan. 2020), p. 013307. DOI: 10.1103/PhysRevE.101.013307.
- [59] A. D. Jagtap and G. E. Karniadakis. “Extended Physics-Informed Neural Networks (XPINNs): A Generalized Space-Time Domain Decomposition Based Deep Learning Framework for Nonlinear Partial Differential Equations”. In: *Communications in Computational Physics* 28.5 (June 2020), pp. 2002–2041. DOI: 10.4208/cicp.0A-2020-0164.
- [60] L. Bar and N. Sochen. “Unsupervised Deep Learning Algorithm for PDE-based Forward and Inverse Problems”. In: abs/1904.0 (2019). DOI: 10.48550/ARXIV.1904.05417.
- [61] S. Bhatnagar et al. “Prediction of aerodynamic flow fields using convolutional neural networks”. In: *Computational Mechanics* 64.2 (Aug. 2019), pp. 525–545. DOI: 10.1007/s00466-019-01740-0.
- [62] Y. Zhu and N. Zabaras. “Bayesian deep convolutional encoder–decoder networks for surrogate modeling and uncertainty quantification”. In: *Journal of Computational Physics* 366 (Aug. 2018), pp. 415–447. DOI: 10.1016/j.jcp.2018.04.018.
- [63] J. Sirignano and K. Spiliopoulos. “DGM: A deep learning algorithm for solving partial differential equations”. In: *Journal of Computational Physics* 375 (Dec. 2018), pp. 1339–1364. DOI: 10.1016/j.jcp.2018.08.029.
- [64] J. Duvall, K. Duraisamy, and S. Pan. “Discretization-independent surrogate modeling over complex geometries using hypernetworks and implicit representations”. In: (2021). DOI: 10.48550/ARXIV.2109.07018.
- [65] H. Gao, L. Sun, and J.-X. Wang. “PhyGeoNet: Physics-informed geometry-adaptive convolutional neural networks for solving parameterized steady-state PDEs on irregular domain”. In: *Journal of Computational Physics* 428 (Mar. 2021), p. 110079. DOI: 10.1016/j.jcp.2020.110079.
- [66] G. Kissas et al. “Learning Operators with Coupled Attention”. In: (2022). DOI: 10.48550/ARXIV.2201.01032.
- [67] L. Lu et al. “A comprehensive and fair comparison of two neural operators (with practical extensions) based on FAIR data”. In: *Computer Methods in Applied Mechanics and Engineering* 393 (Apr. 2022), p. 114778. DOI: 10.1016/j.cma.2022.114778.
- [68] Z. Li et al. “Neural Operator: Graph Kernel Network for Partial Differential Equations”. In: (2020). DOI: 10.48550/ARXIV.2003.03485.
- [69] Z. Li et al. “Fourier Neural Operator for Parametric Partial Differential Equations”. In: (2020). DOI: 10.48550/ARXIV.2010.08895.
- [70] H. You et al. “Nonlocal kernel network (NKN): A stable and resolution-independent deep neural network”. In: *Journal of Computational Physics* 469 (Nov. 2022), p. 111536. DOI: 10.1016/j.jcp.2022.111536.
- [71] T. Chen and H. Chen. “Universal approximation to nonlinear operators by neural networks with arbitrary activation functions and its application to dynamical systems”. In: *IEEE Transactions on Neural Networks* 6.4 (July 1995), pp. 911–917. DOI: 10.1109/72.392253.
- [72] L. Lu et al. “Learning nonlinear operators via DeepONet based on the universal approximation theorem of operators”. In: *Nature Machine Intelligence* 3.3 (Mar. 2021), pp. 218–229. DOI: 10.1038/s42256-021-00302-5.
- [73] S. Cai et al. “DeepM&Mnet: Inferring the electroconvection multiphysics fields based on operator approximation by neural networks”. In: *Journal of Computational Physics* 436 (July 2021), p. 110296. DOI: 10.1016/j.jcp.2021.110296.

- [74] R. Ranade, K. Gitushi, and T. Echekeki. “Generalized Joint Probability Density Function Formulation in Turbulent Combustion using DeepONet”. In: (2021). DOI: 10.48550/ARXIV.2104.01996.
- [75] M. Sharma Priyadarshini, S. Venturi, and M. Panesi. “Application of DeepOnet to model inelastic scattering probabilities in air mixtures”. In: *AIAA AVIATION 2021 FORUM*. Reston, Virginia: American Institute of Aeronautics and Astronautics, Aug. 2021. DOI: 10.2514/6.2021-3144.
- [76] S. Goswami et al. “A physics-informed variational DeepONet for predicting crack path in quasi-brittle materials”. In: *Computer Methods in Applied Mechanics and Engineering* 391 (Mar. 2022), p. 114587. DOI: 10.1016/j.cma.2022.114587.
- [77] Z. Mao et al. “DeepM&Mnet for hypersonics: Predicting the coupled flow and finite-rate chemistry behind a normal shock using neural-network approximation of operators”. In: *Journal of Computational Physics* 447 (Dec. 2021), p. 110698. DOI: 10.1016/j.jcp.2021.110698.
- [78] M. Raissi, P. Perdikaris, and G. Karniadakis. “Physics-informed neural networks: A deep learning framework for solving forward and inverse problems involving nonlinear partial differential equations”. In: *Journal of Computational Physics* 378 (Feb. 2019), pp. 686–707. DOI: 10.1016/j.jcp.2018.10.045.
- [79] G. E. Karniadakis et al. “Physics-informed machine learning”. In: *Nature Reviews Physics* 3.6 (June 2021), pp. 422–440. DOI: 10.1038/s42254-021-00314-5.
- [80] K. Shukla, A. D. Jagtap, and G. E. Karniadakis. “Parallel physics-informed neural networks via domain decomposition”. In: *Journal of Computational Physics* 447 (Dec. 2021), p. 110683. DOI: 10.1016/j.jcp.2021.110683.
- [81] J.-X. Wang, J.-L. Wu, and H. Xiao. “Physics-informed machine learning approach for reconstructing Reynolds stress modeling discrepancies based on DNS data”. In: *Physical Review Fluids* 2.3 (Mar. 2017), p. 034603. DOI: 10.1103/PhysRevFluids.2.034603.
- [82] Z. Mao, A. D. Jagtap, and G. E. Karniadakis. “Physics-informed neural networks for high-speed flows”. In: *Computer Methods in Applied Mechanics and Engineering* 360 (Mar. 2020), p. 112789. DOI: 10.1016/j.cma.2019.112789.
- [83] A. D. Jagtap, E. Kharazmi, and G. E. Karniadakis. “Conservative physics-informed neural networks on discrete domains for conservation laws: Applications to forward and inverse problems”. In: *Computer Methods in Applied Mechanics and Engineering* 365 (June 2020), p. 113028. DOI: 10.1016/j.cma.2020.113028.
- [84] S. Wang, H. Wang, and P. Perdikaris. “Learning the solution operator of parametric partial differential equations with physics-informed DeepONets”. In: *Science Advances* 7.40 (Oct. 2021). DOI: 10.1126/sciadv.abi8605.
- [85] S. Wang and P. Perdikaris. “Long-time integration of parametric evolution equations with physics-informed DeepONets”. In: (2021). DOI: 10.48550/ARXIV.2106.05384.
- [86] S. Wang, H. Wang, and P. Perdikaris. “Improved Architectures and Training Algorithms for Deep Operator Networks”. In: *Journal of Scientific Computing* 92.2 (Aug. 2022), p. 35. DOI: 10.1007/s10915-022-01881-0.
- [87] S. Goswami et al. “Physics-Informed Deep Neural Operator Networks”. In: (2022). DOI: 10.48550/ARXIV.2207.05748.
- [88] Y. Liu, J. N. Kutz, and S. L. Brunton. “Hierarchical deep learning of multiscale differential equation time-steppers”. In: *Philosophical Transactions of the Royal Society A: Mathematical, Physical and Engineering Sciences* 380.2229 (Aug. 2022), p. 20210200. DOI: 10.1098/rsta.2021.0200.
- [89] L. Migus et al. “Multi-scale Physical Representations for Approximating PDE Solutions with Graph Neural Operators”. In: (2022). DOI: 10.48550/ARXIV.2206.14687.
- [90] X. Liu, B. Xu, and L. Zhang. “HT-Net: Hierarchical Transformer based Operator Learning Model for Multiscale PDEs”. In: (2022). DOI: 10.48550/ARXIV.2210.10890.
- [91] L. Liu and W. Cai. “Multiscale DeepONet for Nonlinear Operators in Oscillatory Function Spaces for Building Seismic Wave Responses”. In: (2021). DOI: 10.48550/ARXIV.2111.04860.
- [92] C. Lin et al. “Operator learning for predicting multiscale bubble growth dynamics”. In: *The Journal of Chemical Physics* 154.10 (Mar. 2021), p. 104118. DOI: 10.1063/5.0041203.
- [93] B. Lütjens et al. “Multiscale Neural Operator: Learning Fast and Grid-independent PDE Solvers”. In: (2022). DOI: 10.48550/ARXIV.2207.11417.
- [94] P. Jaysaval et al. “Fully anisotropic 3-D EM modelling on a Lebedev grid with a multigrid pre-conditioner”. In: *Geophysical Journal International* 207.3 (Dec. 2016), pp. 1554–1572. DOI: 10.1093/gji/ggw352.

- [95] Z. Liu, W. Cai, and Z.-Q. J. Xu. “Multi-Scale Deep Neural Network (MscaleDNN) for Solving Poisson-Boltzmann Equation in Complex Domains”. In: *Communications in Computational Physics* 28.5 (June 2020), pp. 1970–2001. DOI: 10.4208/cicp.OA-2020-0179.
- [96] A. Thakur, T. Tripura, and S. Chakraborty. “Multi-fidelity wavelet neural operator with application to uncertainty quantification”. In: (2022). DOI: 10.48550/ARXIV.2208.05606.
- [97] A. A. Howard et al. “Multifidelity Deep Operator Networks”. In: (2022). DOI: 10.48550/ARXIV.2204.09157.
- [98] L. Lu et al. “Multifidelity deep neural operators for efficient learning of partial differential equations with application to fast inverse design of nanoscale heat transport”. In: *Physical Review Research* 4.2 (June 2022), p. 023210. DOI: 10.1103/PhysRevResearch.4.023210.
- [99] A. Munafò et al. “QCT-based vibrational collisional models applied to nonequilibrium nozzle flows”. In: *The European Physical Journal D* 66.7 (July 2012), p. 188. DOI: 10.1140/epjd/e2012-30079-3.
- [100] R. L. Macdonald et al. “Construction of a coarse-grain quasi-classical trajectory method. I. Theory and application to N_2-N_2 system”. In: *The Journal of Chemical Physics* 148.5 (Feb. 2018), p. 054309. DOI: 10.1063/1.5011331.
- [101] R. L. Macdonald et al. “Construction of a coarse-grain quasi-classical trajectory method. II. Comparison against the direct molecular simulation method”. In: *The Journal of Chemical Physics* 148.5 (Feb. 2018), p. 054310. DOI: 10.1063/1.5011332.
- [102] C. Park. *Nonequilibrium Hypersonic Aerothermodynamics*. New York: Wiley, 1990.
- [103] A. Munafò et al. “Reduced-Order Modeling for Non-equilibrium Air Flows”. In: *AIAA Scitech 2020 Forum*. Reston, Virginia: American Institute of Aeronautics and Astronautics, Jan. 2020. DOI: 10.2514/6.2020-1226.
- [104] S. Venturi and T. Casey. “SVD Perspectives for Augmenting DeepONet Flexibility and Interpretability”. In: (2022). DOI: 10.48550/ARXIV.2204.12670.
- [105] G. Berkooz, P. Holmes, and J. L. Lumley. “The Proper Orthogonal Decomposition in the Analysis of Turbulent Flows”. In: *Annual Review of Fluid Mechanics* 25.1 (Jan. 1993), pp. 539–575. DOI: 10.1146/annurev.fl.25.010193.002543.
- [106] X. Li, Y. Grandvalet, and F. Davoine. “A baseline regularization scheme for transfer learning with convolutional neural networks”. In: *Pattern Recognition* 98 (Feb. 2020), p. 107049. DOI: 10.1016/j.patcog.2019.107049.
- [107] S. Wang, Y. Teng, and P. Perdikaris. “Understanding and Mitigating Gradient Flow Pathologies in Physics-Informed Neural Networks”. In: *SIAM Journal on Scientific Computing* 43.5 (Jan. 2021), A3055–A3081. DOI: 10.1137/20M1318043.
- [108] C. Park, R. L. Jaffe, and H. Partridge. “Chemical-Kinetic Parameters of Hyperbolic Earth Entry”. In: *Journal of Thermophysics and Heat Transfer* 15.1 (Jan. 2001), pp. 76–90. DOI: 10.2514/2.6582.
- [109] M. Abadi et al. *TensorFlow: Large-Scale Machine Learning on Heterogeneous Systems*. 2015.
- [110] G. Strang. “On the Construction and Comparison of Difference Schemes”. In: *SIAM Journal on Numerical Analysis* 5.3 (Sept. 1968), pp. 506–517. DOI: 10.1137/0705041.

S. Supplementary Material

S.1. Coarse-grained master equation

As already mentioned in Sec. 2.1.1, this work employs a log-linear form of the distribution function to represent the population within each individual bin, which results in a thermalized local Boltzmann distribution defined as follows:

$$\mathcal{F}_p^i(\epsilon_i): \quad \log\left(\frac{g_i}{n_i}\right) = \alpha_p + \beta_p \epsilon_i . \quad (15)$$

The bin-specific coefficients α_p and β_p are formulated in terms of the macroscopic constraints, total bin population n_p and energy e_p ,

$$n_p = \sum_{i \in \mathcal{S}_p} n_i , \quad e_p = \sum_{i \in \mathcal{S}_p} n_i \epsilon_i , \quad (16)$$

where \mathcal{S}_p indicates the set of internal states contained in the P -th group. The bin internal temperature T_p can be used instead of β_p to characterize the bin distribution function,

$$\beta_p = \frac{1}{k_B T_p} , \quad (17)$$

while the coefficient α_p can then be defined as follows:

$$\alpha_p = \log\left(\frac{Q_p}{n_p}\right) , \quad (18)$$

where Q_p is the group internal partition function,

$$Q_p(T_p) = \sum_{i \in \mathcal{S}_p} q_i(T_p) , \quad (19)$$

with

$$q_i(T_p) = g^e g_i \exp\left(-\frac{\epsilon_i}{k_B T_p}\right) \quad (20)$$

being the i -th level contribution, k_B the Boltzmann's constant, and g^e the degeneracy of the electronic ground state.

S.1.1. Macroscopic equations

Considering the physical framework described in Sec. 2.1.2, the group temperatures T_p are initially assumed to be equal to T_{int_0} and then fixed to the translational temperature for the entire duration of the heat bath. Therefore, only the zeroth-order moment of the master equations is needed to model the reactor dynamics, whose formulation is the same as the StS one,

$$\begin{cases} \frac{dn_p}{dt} = - \sum_{\mathcal{S}_Q \in \mathcal{S}} K_{pQ}^E n_p n_O + \sum_{\mathcal{S}_Q \in \mathcal{S}} K_{Qp}^E n_Q n_O - K_p^D n_p n_O + K_p^R n_O^3 & \forall \mathcal{S}_p \in \mathcal{S} \\ \frac{dn_O}{dt} = \sum_{\mathcal{S}_p \in \mathcal{S}} K_p^D n_p n_O - \sum_{\mathcal{S}_p \in \mathcal{S}} K_p^R n_O^3 \end{cases} , \quad (21)$$

with the state-specific rate coefficients, k_{ij}^E and k_i^D , substituted by the group-specific ones, K_{pQ}^E and K_p^D , obtained from the first as a weighted average based on the Boltzmann distribution function over \mathcal{S}_p

$$K_{pQ}^E(T, T_p) = \sum_{i \in \mathcal{S}_p} \sum_{j \in \mathcal{S}_Q} \frac{q_i(T_p)}{Q_p(T_p)} k_{ij}^E(T) , \quad (22)$$

$$K_p^D(T, T_p) = \sum_{i \in \mathcal{S}_p} \frac{q_i(T_p)}{Q_p(T_p)} k_i^D(T) . \quad (23)$$

The total number density for O_2 is simply the sum of all its bins number densities n_p , while its total internal energy is given by the following summation over the entire set of internal states,

$$e_{O_2} = \sum_{\mathcal{S}_p \in \mathcal{S}} e_p = \sum_{\mathcal{S}_p \in \mathcal{S}} \sum_{i \in \mathcal{S}_p} n_i \epsilon_i = \sum_{\mathcal{S}_p \in \mathcal{S}} \sum_{i \in \mathcal{S}_p} \frac{q_i(T_p)}{Q_p(T_p)} n_p \epsilon_i . \quad (24)$$

S.2. Surrogate details

S.2.1. Hyper-parameter settings

Tab. S1 summarizes the CG-DeepONet architecture (see Sec. 2.2.2), where a modified version of the DeepONet proposed by Wang *et al.* [Eqs. (3.23)-(3.29) in Ref. [86]] is used. The network is trained via mini-batch stochastic gradient descent for 10^4 iterations using the Adam optimizer for each step described in Sec. 2.2.3. The last refinement step using physics-informed optimization techniques has been performed for 5×10^3 epochs. For each training step, to obtain a set of training and validation data, $2 \times N$ initial conditions have been sampled from Tab. 1 using the Latin Hypercube strategy with $N = 2048$. Half of them have been selected as training scenarios using the stratified sampling method, and the remaining half as validation. For each i -th initial condition, $P = 128$ and $P = 32$ data points for training and validation have been log-uniformly sampled in time. To generate the test data set, we randomly sampled 100 unseen initial conditions from Tab. 1 and obtained the corresponding numerical solutions by integrating the ODE using a conventional numerical integrator.

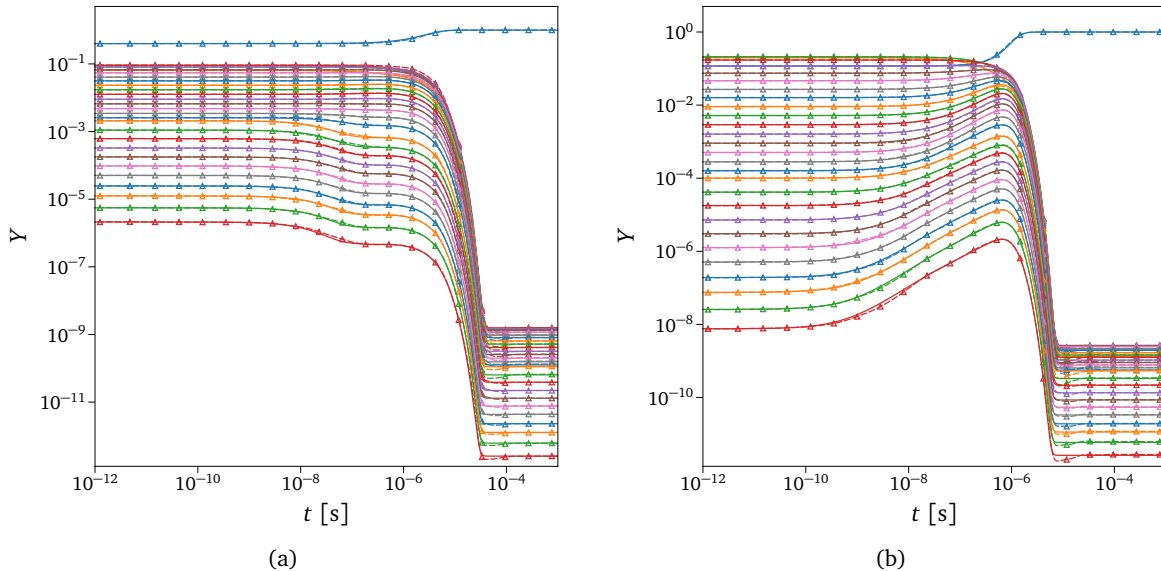
	# DeepONets	Single DeepONet				
		Sub-networks	Type	p	Layers Width	σ
<i>Timescale 1</i>	1	2 Branches	ResFNN	8	[32, 32, p]	tanh \times 3
		1 Trunk	ResFNN		[32, 32, p]	sigmoid \times 3
<i>Timescale 2</i>	1	3 Branches	ResFNN	16	[48, 48, p]	tanh \times 3
		1 Trunk	ResFNN		[48, 48, p]	sigmoid \times 3
<i>Timescale 3</i>	3	3 Branches	ResFNN	16	[48, 48, p]	tanh \times 3
		1 Trunk	ResFNN		[48, 48, p]	sigmoid \times 3
<i>Timescale 4</i>	9	3 Branches	ResFNN	16	[48, 48, p]	tanh \times 3
		1 Trunk	ResFNN		[48, 48, p]	sigmoid \times 3

Table S1. CG-DeepONet architecture. p is the dimension of the features embedding [see Eq. (4)], ResFNN is a novel neural network architecture proposed by Wang *et al.* [Eqs. (2.33)-(2.37) in Ref. [107]], and σ are the activation functions.

It has to be mentioned that an input transformation layer is used to modify the input features. For the trunk net, the time t has been linearly scaled by a factor of 10^7 , while for the branch net, the temperature T has been normalized between 0 and 1. The total number of parameters of the network is 230 106.

S.2.2. Extra test cases

Fig. S1 shows extra testing cases, similarly to what has been shown in Fig. 10.



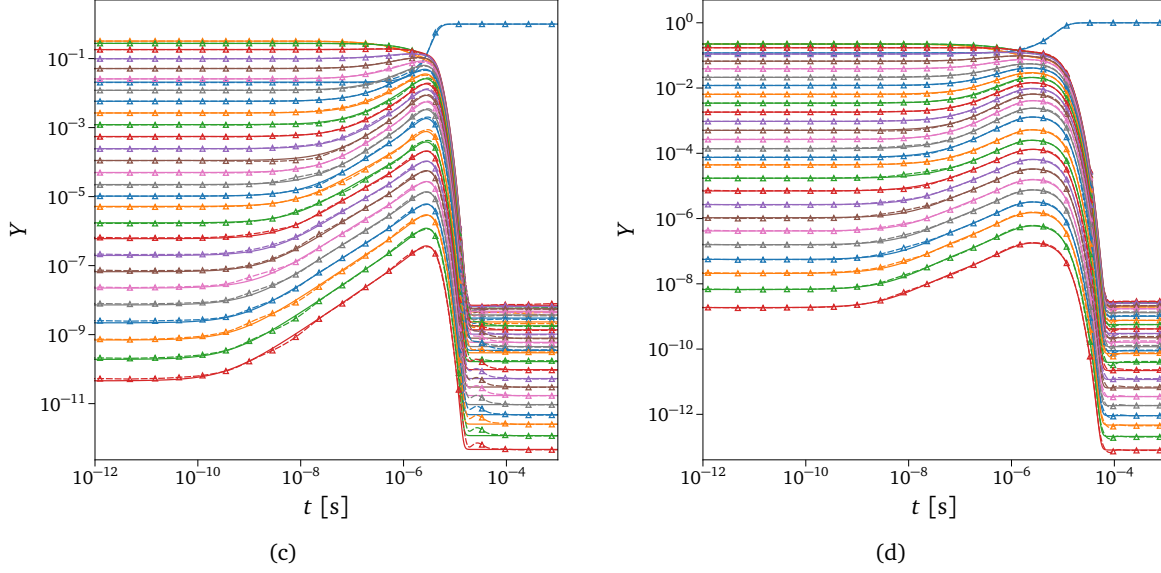


Figure S1. Extra test cases for CG-DeepONets.

S.2.3. Loss histories

In this section, only the last and most interesting refinement step of the training strategy described in Sec. 2.2.3 is presented. Fig. S2(c) shows the evolution of the weights coefficients λ [see Eq. (7)] automatically tuned every 50 iterations with the learning rate annealing technique described by Alg. 2.1 in Ref. [107]. λ_r is fixed and equal to 1 since the ODE residual loss, \mathcal{L}_r , is used as the reference value for computing λ_d and λ_{ic} .

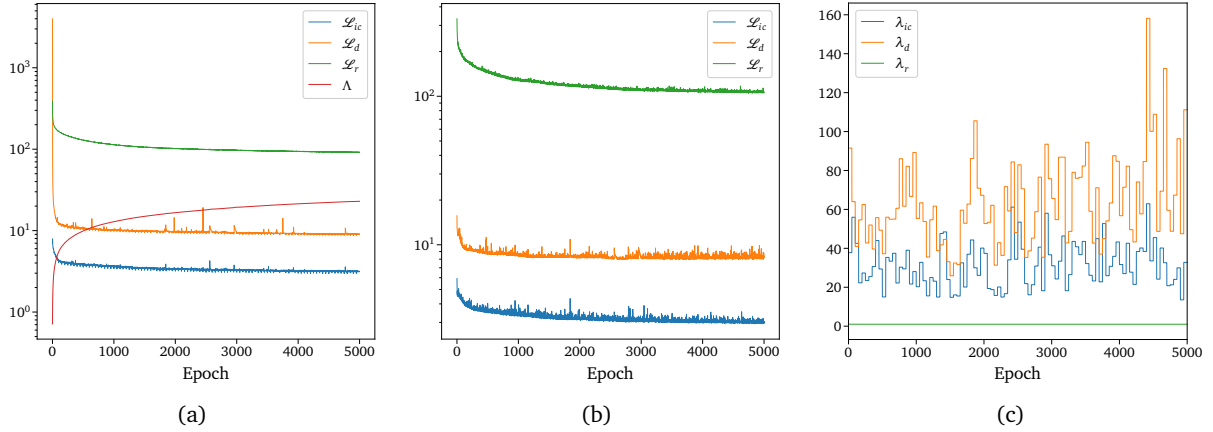


Figure S2. Loss histories of the last physics-informed training step. (a) Training losses. (b) Validation losses. (c) Loss weighting coefficients.

S.3. Adaptive Technique Details

S.3.1. Hyper-parameter settings

Tab. S2 summarizes the Neq-DeepONet architecture (see Sec. 2.3). We trained the model by employing a similar strategy used for the CG-DeepONet, except that all the timescales have been trained simultaneously in this case. The version of the DeepONet used to construct the controller-like surrogate model is an augmented version called *flexDeepONet* proposed by Venturi and Casey [Fig. (8) in Ref. [104]]. The network is trained via mini-batch stochastic gradient descent for 2×10^4 iterations using the Adam optimizer and the mean absolute percentage error as the loss function. How concerns the input transformation layer, for the trunk net, the time t has been linearly scaled by a factor of 10^7 and then log-transformed, while for the branch net, the temperature T has been normalized between 0 and 1. An exponential transformation function is applied to the output of each DeepONet. The total number of parameters of the network is 75 487.

# DeepONets		Single DeepONet				
		Sub-networks	Type	p	Layers Width	σ
<i>Timescale 1</i>	1	1 Branch	FNN	8	$[32, 32, p]$	$\tanh \times 2 + \text{linear}$
		1 Trunk	FNN		$[32, 32, p]$	$\text{sigmoid} \times 2 + \text{linear}$
		1 PreNet	FNN		$[16, 16, 2]$	$\text{sigmoid} \times 2 + \text{linear}$
<i>Timescale 2</i>	1	3 Branches	FNN	16	$[48, 48, p]$	$\tanh \times 2 + \text{linear}$
		1 Trunk	FNN		$[48, 48, p]$	$\text{sigmoid} \times 2 + \text{linear}$
		1 PreNet	FNN		$[16, 16, 2]$	$\text{sigmoid} \times 2 + \text{linear}$
<i>Timescale 3</i>	3	3 Branches	FNN	16	$[48, 48, p]$	$\tanh \times 2 + \text{linear}$
		1 Trunk	FNN		$[48, 48, p]$	$\text{sigmoid} \times 2 + \text{linear}$
		1 PreNet	FNN		$[16, 16, 2]$	$\text{sigmoid} \times 2 + \text{linear}$

Table S2. *Neq-DeepONet architecture*. p is the dimension of the features embedding [see Eq. (4)], FNN is the conventional feed-forward neural network, and σ are the activation functions.

S.3.2. Inference solution and accuracy

In Fig. S3, a comparison between the exact and inferred solutions of the trained model is presented for different test cases, while Tab. S3 reports the four highest errors of the inferred solution, similar to what has been done in Sec. 3.2.

Neq. metric	Rel. error [%]
$\delta^{(3,2,6)}$	1.81 ± 1.50
$\delta^{(3,1,3)}$	1.48 ± 1.34
$\delta^{(2,1,2)}$	1.46 ± 1.25
$\delta^{(3,2,5)}$	1.44 ± 1.24

Table S3. *Neq-DeepONet test error*. The four highest mean relative L^2 -norm testing errors (with standard deviations) of the trained Neq-DeepONet surrogate model.

S.3.3. Adaptive technique algorithm

Alg. 1 presents in detail all the steps of the adaptive technique used to get the inferred solutions as described in Sec. 3.4.

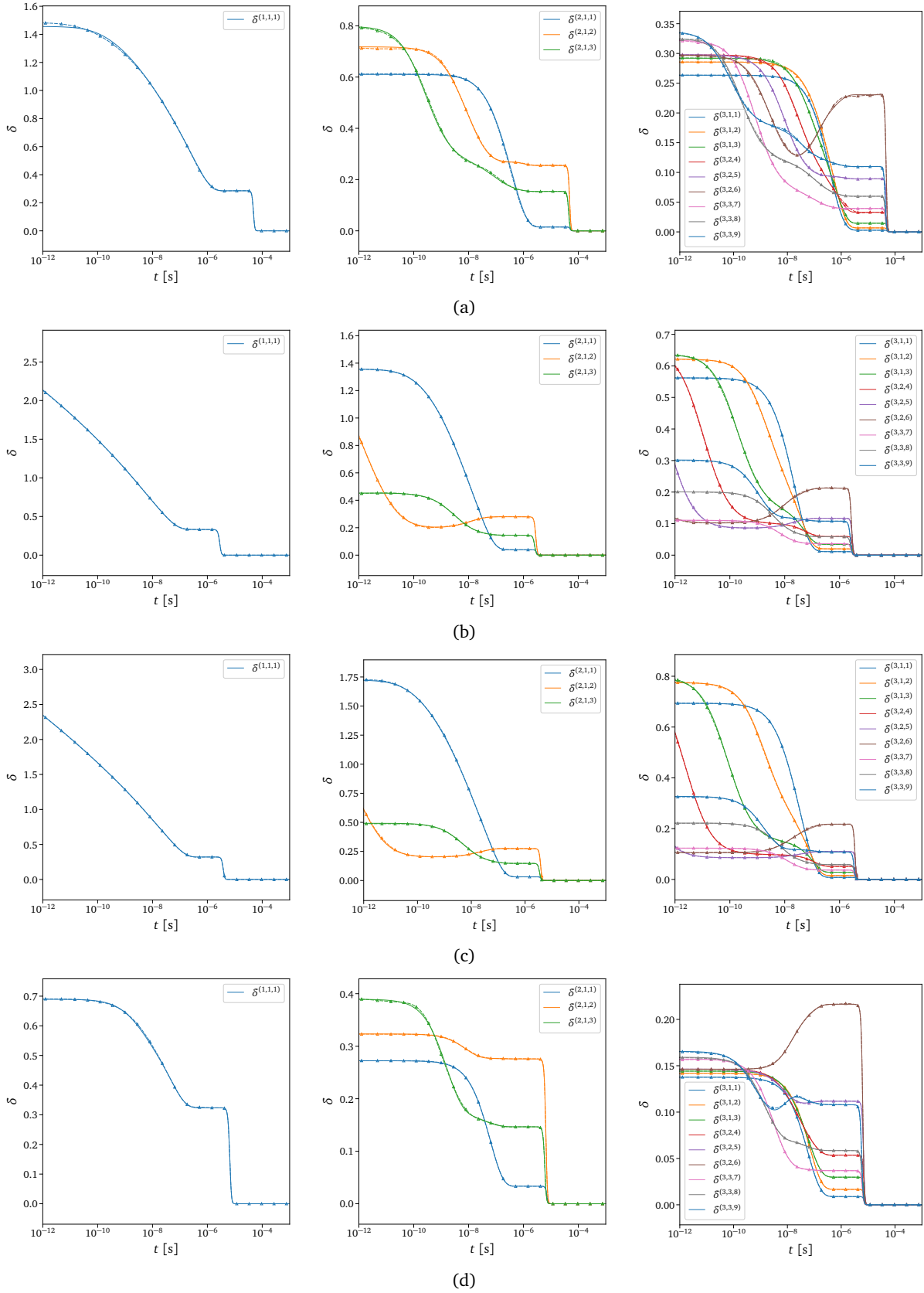


Figure S3. Test cases for Neq-DeepONets. Case (a) is the one shown in Fig. 12.

Algorithm 1: Adaptive technique

Input: Initial conditions matrix and times instants vector

$$X = \left[\left\{ \left(T^i, \rho^i, \mathbf{Y}_{O_2}^i \right) \right\}_{i=1}^n \in \mathbb{R}^{n \times (2 + \mathcal{N}_g)}, \left\{ t^i \right\}_{i=1}^n \in \mathbb{R}^n \right]$$

Output: Mass fractions matrix

$$Y = \left\{ \widehat{\mathbf{Y}}^i \right\}_{i=1}^n \in \mathbb{R}^{n \times (1 + \mathcal{N}_g)}$$

define TS = Number of timescales considered

define δ_{tol} = Underpredicted non-equilibrium tolerance metric

Step 1: Evaluate underpredicted non-equilibrium metric

for $ts = 1, \dots, TS - 1$ **do**

define $\mathcal{N}_{g_{ts}}$ = Number of groups in *Timescale* ts

if $ts = 1$ **then**

 Compute $\delta^{(1,1,1)} \in \mathbb{R}^n$ with Neq-DeepONet^(1,1)

else

if $ts \neq TS - 1$ **and** $all\left(\left\{\delta_i^{(ts-1, \cdot, P)} \leq \delta_{tol}\right\}_{i=1}^n\right) \forall P = 1, \dots, \mathcal{N}_{g_{ts-1}}$ **then**

break

else

for $P = 1, \dots, \mathcal{N}_{g_{ts-1}}$ **do**

define \mathcal{N}_p = Number of micro-groups p contained in macro-group P , $\mathcal{G}_p \subset \mathcal{G}_P$

if $any\left(\left\{\delta_i^{(ts-1, \cdot, P)} > \delta_{tol}\right\}_{i=1}^n\right)$ **then**

- Mask out input data points for which $\left\{\delta_i^{(ts-1, \cdot, P)} \leq \delta_{tol}\right\}_{i=1}^m$ with $m < n$
- Compute $\delta^{(ts, \cdot, P)} \in \mathbb{R}^{n-m} \forall \mathcal{G}_p \subset \mathcal{G}_P$ with Neq-DeepONet^(ts,P)
- Assign $\delta^{(ts, \cdot, P)} = \mathbf{0} \in \mathbb{R}^m \forall \mathcal{G}_p \subset \mathcal{G}_P$

else

 Assign $\delta^{(ts, \cdot, P)} = \mathbf{0} \in \mathbb{R}^n \forall \mathcal{G}_p \subset \mathcal{G}_P$

Step 2: Employ computed underpredicted non-equilibrium metric to evaluate mass fractions

for $ts = 1, \dots, TS$ **do**

define $\mathcal{N}_{g_{ts}}$ = Number of groups in *Timescale* ts

if $ts = 1$ **then**

 Compute $\left\{ \widehat{\mathbf{Y}}_{O_2}, \widehat{\mathbf{Y}}_{O_2}^{(1,1,1)} \right\} \in \mathbb{R}^{n \times 2}$ with CG-DeepONet^(1,1)

else

if $ts \neq TS$ **and** $all\left(\left\{\delta_i^{(ts-1, \cdot, P)} \leq \delta_{tol}\right\}_{i=1}^n\right) \forall P = 1, \dots, \mathcal{N}_{g_{ts-1}}$ **then**

 Reconstruct $\widehat{\mathbf{Y}}_{O_2}^{(TS, \cdot, P)} \in \mathbb{R}^n \forall \mathcal{G}_p \subset \mathcal{G}_P$ from $\widehat{\mathbf{Y}}_{O_2}^{(ts-1, \cdot, P)} \in \mathbb{R}^n \forall P = 1, \dots, \mathcal{N}_{g_{ts-1}}$ by employing the Boltzmann distribution function

break

else

for $P = 1, \dots, \mathcal{N}_{g_{ts-1}}$ **do**

define \mathcal{N}_p = Number of micro-groups p contained in macro-group P , $\mathcal{G}_p \subset \mathcal{G}_P$

if $any\left(\left\{\delta_i^{(ts-1, \cdot, P)} > \delta_{tol}\right\}_{i=1}^n\right)$ **then**

- Mask out input data points for which $\left\{\delta_i^{(ts-1, \cdot, P)} \leq \delta_{tol}\right\}_{i=1}^m$ with $m < n$
- Compute $\widehat{\mathbf{Y}}_{O_2}^{(ts, \cdot, P)} \in \mathbb{R}^{n-m} \forall \mathcal{G}_p \subset \mathcal{G}_P$ with CG-DeepONet^(ts,P)
- Reconstruct $\widehat{\mathbf{Y}}_{O_2}^{(ts, \cdot, P)} \in \mathbb{R}^m \forall \mathcal{G}_p \subset \mathcal{G}_P$ from $\widehat{\mathbf{Y}}_{O_2}^{(ts-1, \cdot, P)} \in \mathbb{R}^m$ by employing the Boltzmann distribution function

else

 Reconstruct $\widehat{\mathbf{Y}}_{O_2}^{(ts, \cdot, P)} \in \mathbb{R}^n \forall \mathcal{G}_p \subset \mathcal{G}_P$ from $\widehat{\mathbf{Y}}_{O_2}^{(ts-1, \cdot, P)} \in \mathbb{R}^n$ by employing the Boltzmann distribution function